Molecular Cell

Resource

Toward community-driven visual proteomics with large-scale cryo-electron tomography of *Chlamydomonas reinhardtii*

Graphical abstract

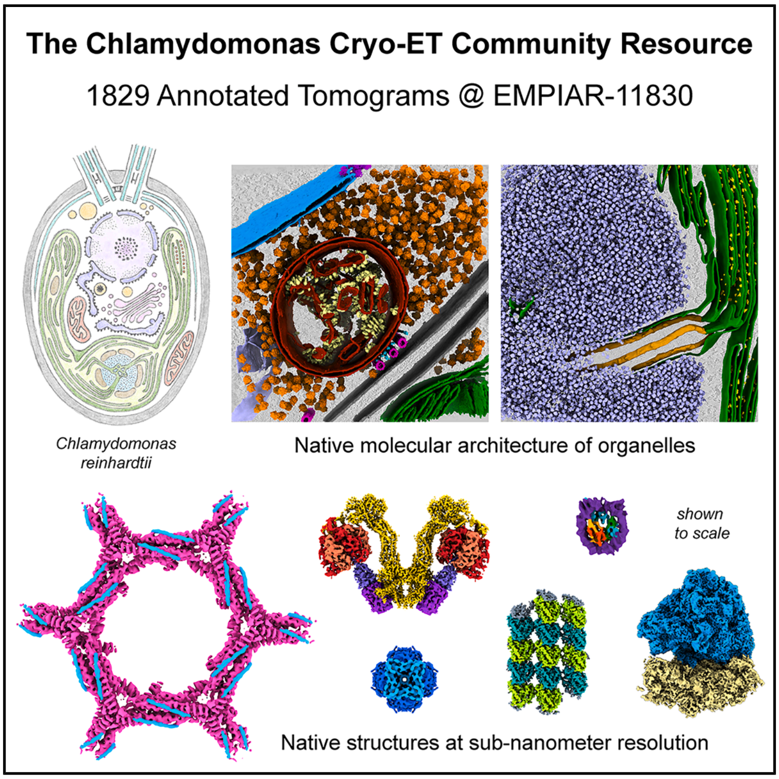

Highlights

- Open community dataset of 1,829 annotated tomograms and raw data
- Molecular visualization of diverse eukaryotic organelles in *C. reinhardtii*
- Data quality assessed by high-resolution subtomogram averaging of native complexes
- An enabling resource to drive biological discovery and method development

Authors

Ron Kelley, Sagar Khavnekar,
Ricardo D. Righetto, ...,
Jürgen M. Plitzko, Benjamin D. Engel,
Abhay Kotecha

Correspondence

ben.engel@unibas.ch (B.D.E.),
abhay.kotecha@stjude.org (A.K.)

In brief

Using the latest advances in instrumentation and computational workflows, Kelley et al. present a large-scale annotated cryo-electron tomography dataset of the model green alga, *Chlamydomonas reinhardtii*. This unprecedented community resource is rich in high-resolution biological information and empowers the development of new methods for visual proteomics.

Kelley et al., 2026, Molecular Cell *86*, 213–230
January 8, 2026 © 2025 The Author(s). Published by Elsevier Inc.
https://doi.org/10.1016/j.molcel.2025.11.029

CellPress

Molecular Cell

CellPress
OPEN ACCESS

Resource

Toward community-driven visual proteomics with large-scale cryo-electron tomography of *Chlamydomonas reinhardtii*

Ron Kelley,[1,9] Sagar Khavnekar,[1,2,9] Ricardo D. Righetto,[3,9] Jessica Heebner,[1,9] Martin Obr,[1,9] Xianjun Zhang,[1,9] Saikat Chakraborty,[1,9,10] Grigory Tagiltsev,[4,9] Alicia K. Michael,[3,5,9] Sofie van Dorst,[3,9] Florent Waltz,[3] Caitlyn L. McCafferty,[3] Lorenz Lamm,[3,6] Simon Zufferey,[3] Philippe Van der Stappen,[3,7] Hugo van den Hoek,[3] Wojciech Wietrzynski,[3] Pavol Harar,[5] William Wan,[8] John A.G. Briggs,[4] Jürgen M. Plitzko,[2] Benjamin D. Engel,[3,12,*] and Abhay Kotecha[1,11,*]

[1]Materials and Structural Analysis Division, Thermo Fisher Scientific, Achtseweg Noord, Eindhoven 5651 GG, the Netherlands
[2]Research Group CryoEM Technology, Max Planck Institute of Biochemistry, Am Klopferspitz 18, 82152 Martinsried, Germany
[3]Biozentrum, University of Basel, Spitastrasse 41, 4056 Basel, Switzerland
[4]Department of Cell and Virus Structure, Max Planck Institute of Biochemistry, Am Klopferspitz 18, 82152 Martinsried, Germany
[5]Institute of Science and Technology Austria, Am Campus 1, 3400 Klosterneuburg, Austria
[6]HelmholtzAI, Helmholtz Munich, Ingolstädter Landstrasse 1, 85764 Neuherberg, Germany
[7]Swiss Nanoscience Institute, University of Basel, Klingelbergstrasse 82, 4056 Basel, Switzerland
[8]Department of Biochemistry and Center for Structural Biology, Vanderbilt University, Nashville, TN 37240, USA
[9]These authors contributed equally
[10]Present address: Division of Structural Biology, Centre for Human Genetics, University of Oxford, Roosevelt Drive, Oxford OX3 7BN, UK
[11]Present address: Center of Excellence for Structural Cell Biology, Department of Structural Biology, St. Jude Children's Research Hospital, 262 Danny Thomas Place, Memphis, TN 38105, USA
[12]Lead contact
*Correspondence: ben.engel@unibas.ch (B.D.E.), abhay.kotecha@stjude.org (A.K.)
https://doi.org/10.1016/j.molcel.2025.11.029

SUMMARY

In situ cryo-electron tomography (cryo-ET) has emerged as the method of choice to investigate the structures of biomolecules in their native context. However, challenges remain for the efficient production and sharing of large-scale cryo-ET datasets. Here, we combined cryogenic plasma-based focused ion beam (cryo-PFIB) milling with recent advances in cryo-ET acquisition and processing to generate a dataset of 1,829 annotated tomograms of the green alga *Chlamydomonas reinhardtii*, which we provide as a community resource to drive method development and inspire biological discovery. To assay data quality, we performed subtomogram averaging of both soluble and membrane-bound complexes ranging in size from >3 MDa to ~200 kDa, including 80S ribosomes, Rubisco, nucleosomes, microtubules, clathrin, photosystem II, and mitochondrial ATP synthase. The majority of these density maps reached sub-nanometer resolution, demonstrating the potential of this *C. reinhardtii* dataset as well as the promise of modern cryo-ET workflows and open data sharing to empower visual proteomics.

INTRODUCTION

The concept of "visual proteomics" was first proposed nearly two decades ago, before instrumentation was developed to enable it.[1] At its heart is the idea of using cryogenic electron tomography (cryo-ET) to produce comprehensive structural inventories of macromolecular complexes inside native cells (*in situ*). The term visual proteomics has since taken on broader interpretations, reflecting the growing potential of integrating cryo-ET with diverse methodologies such as mass spectrometry and AI-based structure prediction.[2] Such efforts are limited by the availability and quality of cryo-ET data, but thanks to advances in instrumentation and computation, cryo-ET is now entering a renaissance where the dream of visual proteomics is beginning to become tangible.[3,4] However, this ambitious goal requires continued developments in (1) data collection to extensively sample cellular environments with high resolution, (2) data analysis to identify and structurally characterize diverse species of macromolecules within these environments, and (3) data sharing in community repositories that enable biological exploration, method development, and training of neural networks.

The quality and throughput of cryo-ET data acquisition have seen substantial improvements in recent years. A crucial sample preparation step for cryo-ET is the thinning of vitreous biological

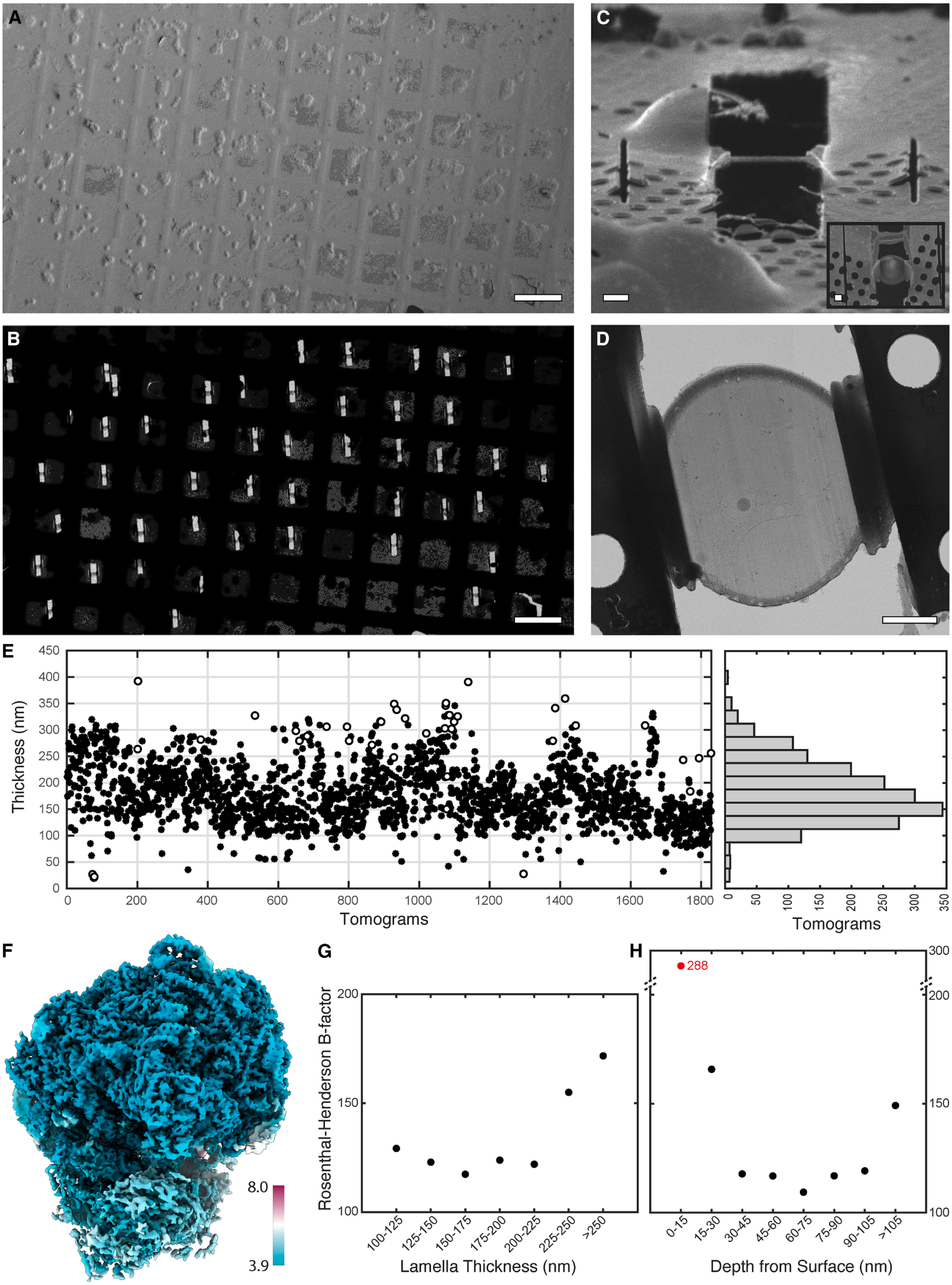

(legend on next page)

material, most commonly performed with a focused ion beam (FIB) to produce cellular "lamellae" with a thickness of ~100–300 nm. Advances in cryo-FIB milling of plunge-frozen and high-pressure-frozen biological material have enabled exploration of diverse cell types[5–12] and even multicellular tissue.[13–15] Throughput has increased by an order of magnitude as a result of automated FIB milling procedures[16–19] and multi-shot cryo-ET, which allows multiple tomograms to be acquired in parallel.[20–24] Despite these gains, the current generation of gallium-based FIB instruments is still limited by manual loading of only two grids at a time, slow milling speeds, and ice contamination on the milled lamella surfaces. A new generation of plasma-based FIB (PFIB) instruments promises to accelerate lamella production.[25] Plasma sources facilitate efficient removal of bulk material from samples ranging from small cells to large volumes of multicellular tissue, which can be advantageous for rough milling steps. In addition, some modern cryo-PFIB systems[25] are equipped with automated liquid nitrogen filling as well as robotic sample handling of up to 12 loaded grids, which enable efficient sample screening, extend the runtimes of automated milling sessions, and can reduce ice contamination introduced by manual handling.

As cryo-ET data output increases, visual proteomics will rely on computational developments aimed at extracting the wealth of information in cellular tomograms. Advances in template matching[26–30] and subtomogram averaging (STA)[28,31–37] have recently enabled the determination of sub-nanometer-resolution structures inside cells for complexes that are relatively large and abundant.[38–41] So far, the most popular targets for *in situ* structural analysis have been ribosomes, which have reached near-atomic resolution (3–4 Å) and enabled classification of numerous native conformational states.[42–47] Alongside these gains in native structure determination, there has been rapid development in automated tomogram segmentation and particle detection within cellular volumes, enabled by increasingly powerful neural networks.[48–52]

However, these AI-based annotation approaches and *in situ* STA both require large and diverse cryo-ET datasets for robust training of generalized neural networks and identifying enough examples of less abundant macromolecular species to allow high-resolution averaging. Public data repositories, such as the Electron Microscopy Public Image Archive (EMPIAR)[53] and the Chan Zuckerberg Imaging Institute (CZII) Cryo-ET Data Portal,[54] aim to aggregate cryo-ET datasets from the global research community to enable method development and biological discovery. Yet to date, very few large-scale datasets of cellular cryo-ET are available.

Here, we provide a new resource to enable community-driven efforts toward visual proteomics. Using an efficient workflow that combines cryo-PFIB milling with high-resolution cryo-ET, we produced an open community dataset of 1,829 curated tomograms (and accompanying raw data) covering the breadth of organelles found within *Chlamydomonas reinhardtii* cells. These unicellular green algae are ideal models for cryo-ET, thanks to their small size (compatible with plunge-freezing vitrification and high-throughput FIB milling), good cryo-ET contrast, and reproducible cellular architecture, with a cornucopia of eukaryotic structural cell biology to explore.[55] Furthermore, *C. reinhardtii* benefits from a wealth of molecular tools and mutant libraries,[56,57] as well as an active research community using this model organism to study diverse questions, including cilia biology and photosynthesis.[58–60] To test the feasibility of structure determination from our dataset, we performed STA of a variety of native macromolecules ranging in size from ~200 kDa to >3 MDa, including both soluble and membrane-integral complexes. It is our hope that this publicly available *C. reinhardtii* dataset will empower new discoveries and method development while providing an example for open sharing of future large-scale datasets generated by the rapidly growing cryo-ET community.

RESULTS

Cryo-PFIB milling to enable large-scale cryo-ET

We leveraged the automated features of the recently developed Arctis cryo-PFIB to increase the throughput of lamella production. Each session, we used the autoloader and multi-specimen cassette to screen 8–10 grids with vitrified *C. reinhardtii* cells before beginning milling. The suitability of each grid was assessed with scanning electron microscopy (SEM) atlas overviews (Figures 1A and S1A). Grids with sufficient coverage of isolated single cells or clusters of up to three cells, close to the center of the grid square and with minimal frozen buffer surrounding the cells, were chosen for further processing. Grids that had larger clumps of cells or a thicker ice layer were discarded, as such material is unlikely to be completely vitrified.

Our PFIB system was equipped with xenon, argon, and oxygen ion sources, each offering distinct properties. Characterization of milling with different ion species has shown some differences,[61] including higher sputter rates when milling with xenon. While cryo-FIB/SEM volume imaging and lamella

Figure 1. High-throughput cryo-ET workflow applied to *C. reinhardtii*

(A) SEM image of an EM grid covered in frozen *C. reinhardtii* cells.

(B) Low-magnification TEM image of the grid with lamellae that were prepared by cryo-PFIB milling.

(C) Ion beam image of a single lamella as seen from the milling angle. Inset: SEM top view of the lamella.

(D) TEM overview search map of a single lamella.

(E) Plot of tomogram thickness for the full dataset (EMPIAR: EMPIAR-11830), summed into the histogram on the right. Tomogram thickness was determined by two methods (black circles: TOMOMAN functionality that uses IMOD's findsection program; white circles: Slabify; see STAR Methods).

(F) Local-resolution display of the 80S ribosome subtomogram average, with the large subunit at Nyquist resolution (3.92 Å).

(G) Dependence of 80S ribosome B-factor (units: Å^2) on lamella thickness.

(H) Dependence of 80S ribosome B-factor on the distance of particles from the lamella surface. Note that the 0–15 nm bin (red point) contains partial ribosomes that were cut by FIB milling, thus resulting in a much higher B-factor. The 15–30 nm bin contains complete ribosomes but a higher B-factor than deeper bins spanning 30–105 nm, likely due to beam damage near the lamella surface. Scale bars: 100 μm in (A) and (B); 1 μm in (C), (C, inset), and (D).

See also Figures S1–S3.

preparation have traditionally utilized either gallium or argon ion beams,[16,25,62–64] a recent study demonstrated the successful use of xenon for milling high-pressure-frozen biological samples.[65] In this work, the majority of lamellae were milled with xenon, but we also milled a smaller set of lamellae using argon to compare the milling throughput. The average time to prepare a lamella from *C. reinhardtii* cells with xenon ions was ∼23 min, including 4 min site preparation time and 19 min milling time (Table S1). Lamellae prepared with argon ions averaged ∼26 min per site, with 4 min site preparation time and 22 min milling time (Table S2). Overall, we found that xenon was marginally faster for milling lamellae from plunge-frozen *C. reinhardtii* cells. Depending on the number of available cells, between 10 and 40 lamellae were prepared on each grid (Figures 1B–1D) with an automated milling rouine using AutoTEM[19] or WebUI[66] software. The target width of each lamella was 8–10 µm, and the target thickness was 150–200 nm.

Grids with lamellae were transferred to the Krios transmission electron microscopy (TEM) directly from the Arctis cryo-PFIB using the same cassette and capsule setup, eliminating manual handling steps and, thereby, reducing the risks of ice contamination and lamella breakage during the transfer process. This direct transfer prevents grid rotation between the two instruments, ensuring that lamellae are in the correct orientation for tilt-series collection, with the FIB milling direction roughly perpendicular to the TEM tilt axis (Figures S1B and S1C). Across 42 overnight imaging sessions, we acquired a dataset of 2,991 tilt series from 55 different grids containing over 300 lamellae. As a trade-off between cellular coverage and resolution, we selected a pixel size of 1.96 Å, setting the Nyquist limit at 3.92 Å. All tilt series and their individual tilt images were manually curated and then processed through an automated alignment and reconstruction pipeline. Tilt series that suffered from non-vitreous ice and alignment issues were discarded. In total, 1,829 reconstructed tomograms were deemed to be of good quality for further analysis. The high discard rate was primarily the result of inconsistent sample quality, with some grids containing mostly non-vitreous cells. We measured the thicknesses of all the retained tomograms, which varied from ∼100 to ∼300 nm (excluding ∼10% outliers), with a median thickness of 157 nm (Figure 1E). To aid visual inspection, segmentation, and particle picking, all tomograms were denoised using cryo-CARE software.[67]

Analysis of radiation damage from PFIB using 80S ribosomes

Recently, sub-5 Å STA maps of 80S ribosomes were obtained from cryo-ET data acquired on cells milled using cryo-PFIB milling.[25,68] Several functional states of the 80S ribosome complex were resolved from these datasets using classical[28] as well as machine learning-based[68] approaches. Here, we used *C. reinhardtii* 80S ribosome particles to assess the dependence of attainable resolution on lamella thickness and PFIB-induced beam damage to the lamella surface. We first used a small subset of ∼6,000 subvolumes extracted from 16 tomograms (from the initial acquisition sessions) and obtained a ribosome structure with a global resolution of 5.5 Å (Figure S2B). We then expanded our dataset to ∼140,000 subvolumes from 600 tomograms and obtained a 4.0 Å STA map, with resolution of the ribosomal large subunit extending to the Nyquist limit (3.9 Å) (Figures 1F and S2D). In addition, the large size of the dataset allowed us to use subvolume classification (Figure S2E) to distinguish free cytosolic ribosomes (in complex with ES27 and Arx1) from ribosomes bound to the endoplasmic reticulum (ER) membrane (in complex with sec61-TRAP) (Figure S2F),[69] as well as different functional states with resolved occupancies for tRNA and elongation factors (Figure S2G).

Recent studies have demonstrated that gallium and argon ion beams damage the lamella surface during cryo-FIB milling.[25,70,71] We analyzed Rosenthal-Henderson B-factors[72] for 80S ribosome averages generated from lamellae with varying thicknesses and observed that thicker lamellae (>225 nm) had a reduced signal-to-noise ratio (SNR) (Figures 1G and S3A). Although this suggests that it is beneficial to mill thinner lamellae for high-resolution imaging, further B-factor analysis for ribosomes at varying depths within lamellae indicated a damage layer extending up to 30 nm from the lamella surface (Figures 1H and S3B), consistent with previous reports.[25,71] It's important to note that this analysis has inherent limitations due to the size of 80S ribosomes, which are ∼30 nm in diameter. Therefore, the high B-factor value (288 Å^2) for particles 0–15 nm from the surface is due to incomplete ribosomes that were cut by FIB milling. However, the 15–30 nm bin has a higher B-factor (166 Å^2) than the 30–45 nm bin (118 Å^2), indicating that indeed particles 15–30 nm from the lamella surface incur some damage. The B-factors remain relatively constant between 30 and 105 nm but increase again in the 105+ nm bin, likely due to reduced SNR in thicker lamellae. From this analysis, we conclude that *C. reinhardtii* lamellae of <225 nm thickness are best for high-resolution STA, using particles positioned approximately 30–100 nm from the lamella surface.

Toward visual proteomics in *Chlamydomonas*

C. reinhardtii has characteristic cellular architecture, which has enabled *in situ* cryo-ET studies of the nucleus (including the nucleolus and nuclear pores),[73–75] ER,[69,76] Golgi and secretory system,[77–79] centrioles and cilia,[80–84] actin filaments,[85] mitochondria,[86,87] and chloroplasts (including pyrenoid and thylakoids).[88–91] To gain an overview of this cellular architecture, we first used a Hydra cryo-PFIB to perform slice-and-view volume EM imaging of an entire vitreous *C. reinhardtii* cell (Figures 2A, S1D, and S1E). This method, traditionally established for resin-embedded biological samples[92,93] and recently demonstrated for cryo applications,[62,64] works by sequentially removing material with the ion beam and imaging the newly created cross-section surfaces with the scanning electron beam to obtain a 3D volume. The resulting overview of a full *C. reinhardtii* cell helped provide orientation when examining low-magnification search images of lamellae from other cells in the TEM (Figure 2B), guiding the selection of positions for tilt-series acquisition. The 1,829 tomograms in the curated dataset contain the following organelles (sometimes with multiple organelles in one tomogram): 387 tomograms of the nucleus (Figure 2C), 246 of the Golgi apparatus (Figure 2D), 16 of centrioles (Figure 2E), 581 of mitochondria (Figure 2F), and 823 of the chloroplast (Figure 2G), including 84 of the pyrenoid

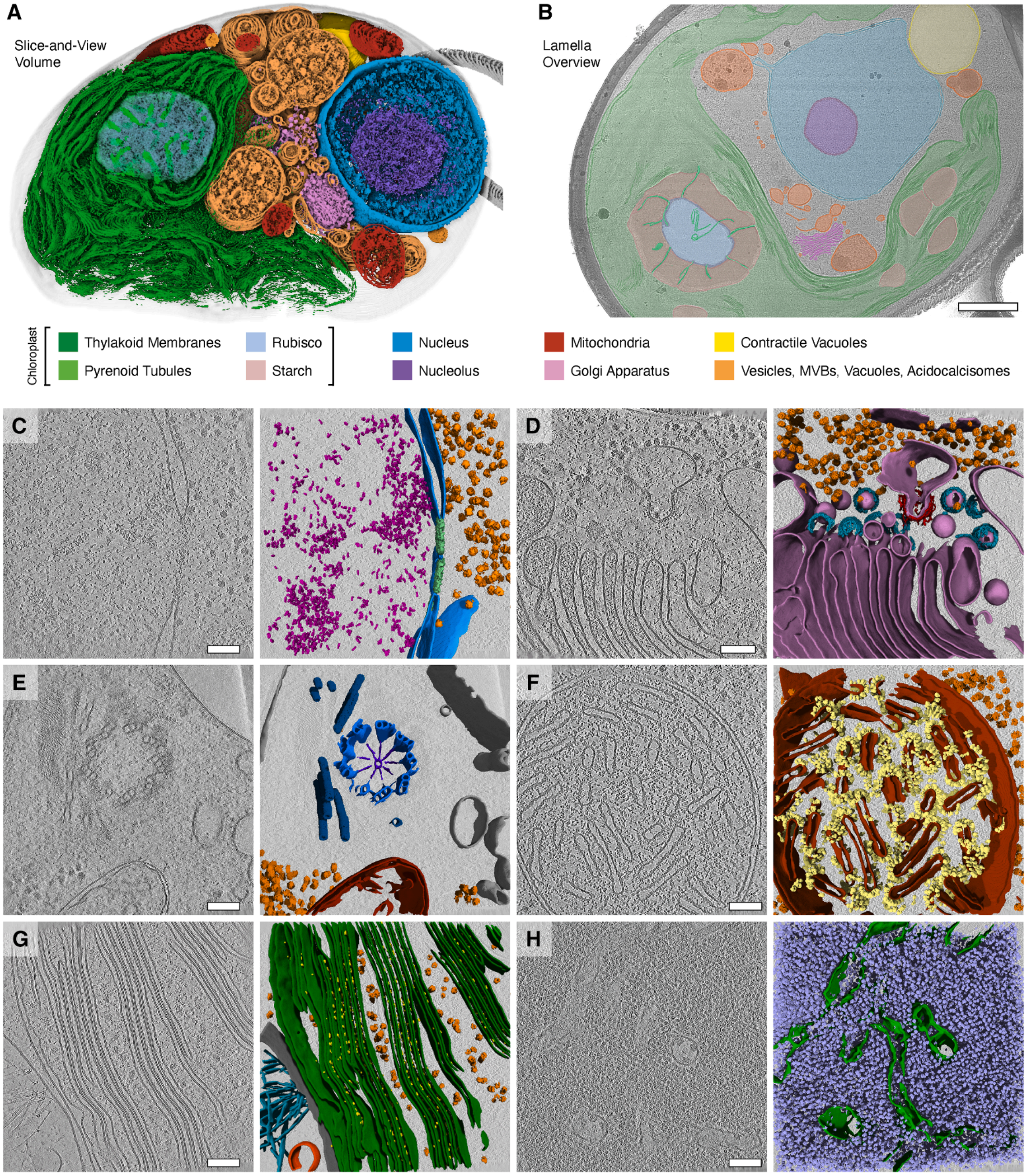

Figure 2. Molecular architecture of *C. reinhardtii* cellular compartments found in the large-scale cryo-ET dataset

(A) 3D segmentation of a whole vitreous *Chlamydomonas* cell imaged by cryo-PFIB/SEM slice-and-view (EMPIAR: EMPIAR-11275) highlighting overall cellular architecture. 20 nm slice thickness, 335 slices covering about 6.7 μm^3 of cell volume. See also Figures S1D and S1E.

(B) TEM search image of a lamella with major structures colored by indentity. Scale bar: 1 μm. Color legend applies to (A) and (B).

(C–H) Slices through representative tomograms of cellular compartments (left) with corresponding 3D segmentations (right). Scale bars: 100 nm. (C) Nucleus, with segmented nuclear envelope (blue), nucleosomes (magenta), 80S ribosomes (orange), and a nuclear pore complex (green); Tomo #649. (D) Golgi apparatus, with segmented Golgi and ER membranes (pink), 80S ribosomes (orange), COPII (red), and COPI (cyan); Tomo #50.

(E) Basal body (i.e., centriole), with segmented membranes (gray), mitochondria (red), MT triplets (blue), cartwheel (indigo), 80S ribosomes (orange), and rootlet MTs (navy); Tomo #2836.

(F) Mitochondria, with segmented mitochondrial membranes (red), ATP synthases (pale yellow), and 80S ribosomes (orange); Tomo #167.

(G) Chloroplast, with segmented thylakoid membranes (green), PSII (yellow), 70S and 80S ribosomes (orange), membrane (gray), filaments (cyan), and a vesicle (deep orange); Tomo #909.

(H) Pyrenoid, with segmented pyrenoid tubule membranes (green) and Rubisco (lavender blue); Tomo #2162.

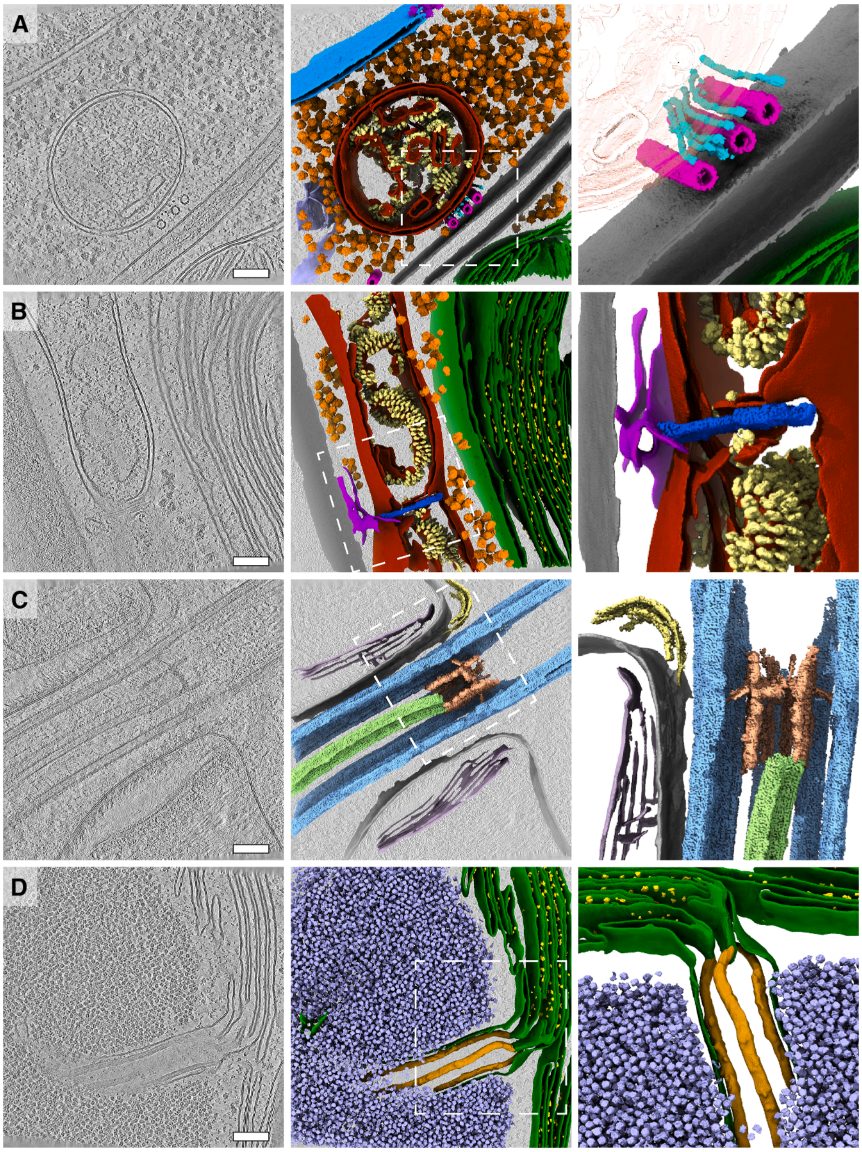

Figure 3. Rare cellular events observed in the cryo-ET dataset

Slices through tomograms (left) with corresponding 3D segmentations (middle and right). Right panels show enlarged views of the boxed regions in the middle panels.

(A) Mitochondrion at the plasma membrane, tethered to MTs by thin filaments of unknown identity. Segmented classes: nuclear envelope (light blue), nuclear pore complex (purple), 80S ribosomes (orange), mitochondrial membranes (dark red), ATP synthases (pale yellow), plasma membranes (gray), MTs (pink), filaments (cyan), and chloroplast membranes (green). The zoomed-in panel on the right shows thin filaments running between MTs and the mitochondrion (transparent red) at the plasma membrane. Note that this tomogram contains two closely appressed cells, and thus, two plasma membranes with cell walls in between; Tomo #298.

(B) Mitochondrial fission event with ER membrane interactions. Segmented classes: mitochondrial membranes (dark red), ATP synthases (pale yellow), 80S ribosomes (orange), chloroplast membranes (green), PSII (bright yellow), cell wall (gray), ER (purple), and fission site containing filamentous structures perpendicular to the mitochondrial long axis (blue); Tomo #2917.

(C) Ciliary transition zone between basal body and axoneme, including assembling IFT train and stellate structure.[82] Segmented classes: MT triplets and doublets (light blue), central pair MTs (light green), stellate structure (pale red), IFT train (yellow), plasma membrane and ciliary membrane (gray), and flagellar collar (lavender gray); Tomo #2803.

(D) Pyrenoid tubule extending from the thylakoids into the phase-separated Rubisco matrix of the pyrenoid. Minitubules originate from thylakoid membranes.[88] Segmented classes: thylakoid membranes and pyrenoid tubule (dark green), pyrenoid minitubules (light orange), PSII (bright yellow), and Rubisco (lavender blue); Tomo #929. Scale bars in (A)–(D): 100 nm.

compartment (Figure 2H). In addition, microtubules (MTs), actin, ER, multivesicular bodies (MVBs), and a variety of acidocalcisomes and other vacuoles are also present in the dataset. We trained several 2D, 2.5D, and 3D U-nets on a small subset of the data to enable semi-automated semantic segmentation of this cellular ultrastructure[49,94,95] (Figures 2C–2H and 3).

Our deep sampling of *C. reinhardtii* cellular architecture provided views of specific and transient organelle features. For example, we observed a mitochondrion bound to three MTs via thin filaments (Figure 3A), as well as a mitochondrion undergoing a putative fission event mediated by contact with the ER (Figure 3B).[96] We also acquired tomograms of the ciliary transition zone with assembling intraflagellar transport (IFT) trains (Figure 3C)[82–84] and captured detailed views of the pyrenoid tubules and thylakoid-derived minitubules (Figure 3D), enigmatic structures that are not fully understood on a molecular level.[88,97–99]

STA of diverse molecular complexes

Cytosolic ribosomes have received considerable attention in recent *in situ* cryo-ET studies, as their abundance and large size enable high-resolution structure determination of numerous functional states.[42–46] Indeed, ribosomes were also our first target when benchmarking the quality of our dataset (Figures 1F–1H, S2, and S3). However, one of the main aims of producing a large-scale dataset covering a range of *C. reinhardtii* organelles is to enable structural studies of diverse molecular targets within the native cellular environment, taking a step toward visual proteomics. To assess the potential of our dataset, we performed STA of six molecular complexes that varied in size, properties, and cellular location (Figure 4). To test smaller soluble complexes, we averaged ~520 kDa Rubisco enzymes in the pyrenoid subcompartment of the chloroplast and ~200 kDa nucleosomes in the nucleus. To test oligomeric assemblies, we averaged MT filaments and clathrin coats in the cytosol. Finally, to test

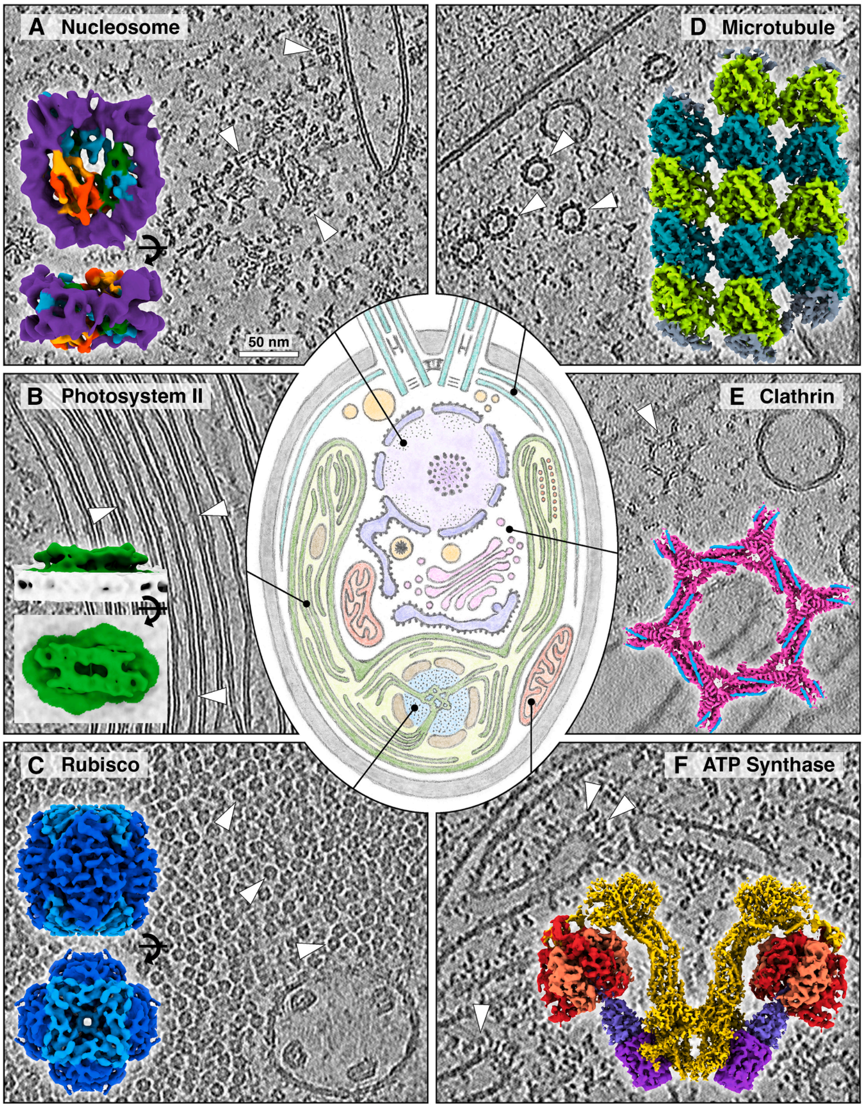

Figure 4. Visualizing molecular machinery inside native *C. reinhardtii* cells

Central illustration: stereotypical cross-section through a *Chlamydomonas* cell (teal: rootlet MTs and centrioles attached to cilia; darker purple: nuclear envelope and ER; light purple: nucleoplasm with chromatin at periphery and nucleolus at center; pink: Golgi and associated vesicles; light orange: assorted vacuolar compartments including acidocalcisome with dark granule and contractile vacuoles near centrioles; darker green: chloroplast envelope and thylakoids; light green: chloroplast stroma; blue: pyrenoid Rubisco matrix; brown: starch; darker orange: eyespot granules; darker red: mitochondrial envelope and cristae; light red: mitochondrial matrix; gray: cell wall). Surrounding panels: slices through example tomograms (grayscale), with positions of the molecular complexes marked (arrowheads), and STA density maps of those complexes overlaid (in color). Scale bar: 50 nm; all tomograms shown at the same scale.

(A) Nucleosomes in the nucleus. STA map: 9.6 Å resolution, purple: DNA, orange: histone H2A, red: histone H2B, blue: histone H3, green: histone H4. See also Figure S5.

(B) PSII embedded within thylakoid membranes of the chloroplast. STA map: 19 Å resolution, green: PSII, gray: membrane. See also Figure S8.

(C) Rubisco in the pyrenoid compartment of the chloroplast. STA map: 7.5 Å resolution, dark blue: Rubisco large subunits, light blue: Rubisco small subunits. See also Figure S4.

(D) MTs in the cytoplasm. STA map: 4.7 Å resolution, light and dark green: tubulin monomers. See also Figure S6.

(E) Clathrin lattice in the cytoplasm. STA map: 8.7 Å resolution, pink: clathrin heavy chains, blue: clathrin light chains. See also Figures 5A, 5B, and S7.

(F) ATP synthase dimers embedded in the crista membranes of mitochondria. Composite STA map: peripheral stalk (yellow) at 5.2 Å resolution, F_1 head (shades of red) at 8.5 Å resolution, purple: F_0 rotor ring, blue: central stalk.
See also Figures 5C–5H and S9.

membrane protein complexes, we averaged ~600 kDa photosystem II (PSII) complexes in the thylakoid membranes of the chloroplast and ~1.3 MDa dimers of ATP synthase in the crista membranes of the mitochondria. Five of these averages (all except PSII) reached sub-nanometer resolution, revealing secondary structure features. As detailed in the methods, each of the STA projects was performed by a different user, using a range of computational workflows and software packages for particle picking, alignment, and refinement, thereby demonstrating the utility of the *C. reinhardtii* dataset for a variety of analysis pipelines.

Rubisco in the chloroplast

Rubisco enzymes perform carbon fixation, assimilating CO_2 into sugar. Green algae such as *C. reinhardtii* contains type-I Rubisco, a ~520 kDa holocomplex composed of eight large subunits and eight small subunits. *C. reinhardtii* increases the efficiency of CO_2 fixation by densely packing Rubisco into a chloroplast microcompartment called the pyrenoid, which forms by liquid-liquid phase separation and is traversed by a network of membrane tubules (Figures 2H and 3D).[88,89] The high concentration of Rubisco particles within the pyrenoid provides an opportunity to test STA workflows for relatively rigid and small particles immersed in a crowded cellular environment.

Despite the dense packing of particles, discrete Rubisco holocomplexes were clearly visible within tomograms of the pyrenoid (Figures 4C and S4A). We implemented a template matching workflow using a template density simulated from a crystal structure,[100] which we used to pick ~240,000 particles from the dataset (Figure S4B). After STA with multireference alignment, we obtained a 7.5 Å-resolution map (Figures 4C, S4D, and S4E) from a class containing ~14,000 particles (6% of the initial picks; Figure S4C). This small percentage of picked subvolumes (including many true-positive Rubisco particles from visual inspection) that made it into the final high-resolution average highlights the challenges to template matching and subtomogram alignment posed by molecular crowding *in situ*. It is also likely that the particles within the pyrenoids are more heterogeneous than we had originally expected, due to Rubisco binding partners such as Rubisco activase and the linker protein EPYC1.[101,102] Continued computational developments are required to better resolve the majority of small particles in such a crowded environment.

Nucleosomes in the nucleus

Like in plants and animals, the nuclear genome of *C. reinhardtii* is packaged into chromatin. The fundamental unit of chromatin is the nucleosome, an octamer of histone proteins wrapped with ~147 base pairs of DNA.[103] Nucleosomes are exciting targets for *in situ* cryo-ET because resolving their native structures and organization within cells has the potential to provide fundamental new insights into gene regulation. However, nucleosomes are relatively small (~200 kDa), and the nucleus is densely packed with DNA and other macromolecules, making it difficult to unambiguously pinpoint specific structures in tomograms. Consequently, published structures of nucleosomes within cells have been limited to a maximum resolution of ~12 Å.[104–108] *C. reinhardtii* has the advantage of a smaller nuclear genome (120 Mb compared with 6.27 Gb in human cells), and nuclear tomograms show a relatively sparse distribution of macromolecules (Figure 4A), making it a promising model system for structural investigations of native nuclear complexes.

Using template matching and STA, we determined the nucleosome structure in *C. reinhardtii* at sub-nanometer resolution within the cell. Not only does the relatively small size of the nucleosome make it a challenging target, but the wrapping DNA, which is denser than protein, causes the side views to be more prone to detection than the top and bottom views, skewing the angular distribution of the picked particles (Figure S5G). Similar to our analysis of Rubisco, only ~11% of particles picked by template matching were retained in our final average after classification (~24,000 out of ~224,000 particles; Figures S5C and S5D), highlighting the challenge of studying small complexes within crowded environments. Nevertheless, a global resolution of 9.6 Å was achieved, revealing secondary structure elements within the histone core, including defined α-helices (Figures S5F, S5H, and S5I). At this resolution, the helical turns of DNA begin to be visible (Figure 4A). We observe additional diffuse density near the nucleosome dyad and entry/exit site, known hotspots for interaction, which can likely be attributed to a mixture of bound factors. Classifying the heterogeneity of nucleosome states and interactions remains an opportunity for future studies.

Microtubules in the cytosol

The cytoplasmic MTs of *C. reinhardtii* are nucleated near the centrioles and extend around the periphery of the cell. In our dataset, we observed both single MTs and bundles of 3–4 MTs, perhaps corresponding to the cortical and rootlet MTs, respectively.[109,110] MT protofilaments were clearly discernible in cross-section and side views (Figures 4D and S6A). *C. reinhardtii* cytoplasmic MTs have 13 protofilaments, the canonical number of protofilaments that is also observed in mammalian cells.[111] This conservation is noteworthy, as a diversity of protofilament number has been observed in some other species, including 11 and 15 in *C. elegans* worms[13,112] and 13–18 in malaria parasites.[5] Recent *in situ* cryo-ET studies of mammalian neurons and pluripotent cells have produced STA maps of 13-protofilament MTs with resolutions ranging from 12 to 8.2 Å.[113,114] We therefore proceeded to average the MTs we found in the *C. reinhardtii* dataset to benchmark the quality with which we could resolve these conserved cytoskeletal structures.

After extracting particles along traced MT filaments and performing an STA strategy that accounts for MT geometry and polarity, we obtained a 4.7 Å-resolution map of the *C. reinhardtii* MT lattice from only ~15,000 subvolumes (Figures 4D and S6B–S6G). The map shows clear secondary structural elements, including α helices and β strands (Figure S6H). Notably, our STA revealed that cytoplasmic MTs have uniform polarity orientations in all tomograms, consistent with a polarized cytoskeleton nucleated at the apical end of the cell near the centrioles. This polarity is comparable to the axonal MT cytoskeleton observed by cryo-ET of mammalian neurons.[114]

Clathrin coats in the cytosol

Clathrin is involved in the budding of coated vesicles on the plasma membrane, the *trans*-Golgi network, and endosomes. Upon recruitment to the membrane by adaptor proteins, clathrin forms a lattice-like coat composed of a mixture of pentagons, hexagons, and heptagons. It has a characteristic triskelion geometry consisting of three heavy chains (~190 kDa) and three light chains (~25 kDa). While clathrin has not been extensively studied in *C. reinhardtii*, its sequence is well conserved between *C. reinhardtii* and mammals, and the mammalian structure has been determined to high resolution *in vitro*[115] and to low resolution *in situ*.[116] We identified ~6,000 clathrin triskelia using template matching and subsequent cleaning. These particles were fed into an STA pipeline, yielding a final 8.7 Å-resolution map from ~18,000 C1-symmetric particles (Figures 4E and S7A–S7G). At this resolution, the *in situ* map is similar to the previously reported *in vitro* structures, implying high structural conservation between mammals and green algae and confirming that the *in vitro* structures are biologically representative.

Placing the clathrin structure back into the tomograms revealed clathrin assemblies at various stages of vesicle maturation, ranging from budding clathrin-coated pits to mature clathrin-coated vesicles. These assemblies displayed a variety of clathrin lattice polygonal architectures, including pentagons, hexagons, and heptagons (Figures 5A, 5B, and S7H). In addition to visualizing and characterizing the native lattice organization, structural work on clathrin *in situ* may allow the roles of interacting factors in lattice assembly and disassembly to be assessed. The potential for localizing and resolving different components of the clathrin pathway in action within the cell remains to be explored, potentially using this *C. reinhardtii* dataset.

Photosystem II in the chloroplast

Resolving membrane proteins remains a major challenge for cryo-ET. The high-atomic-weight phosphate head groups of lipid bilayers create a strong signal in TEM, which interferes with the analysis of membrane-embedded protein domains both in particle picking and the alignment of subtomograms. We therefore decided to test our *C. reinhardtii* dataset for the feasibility of

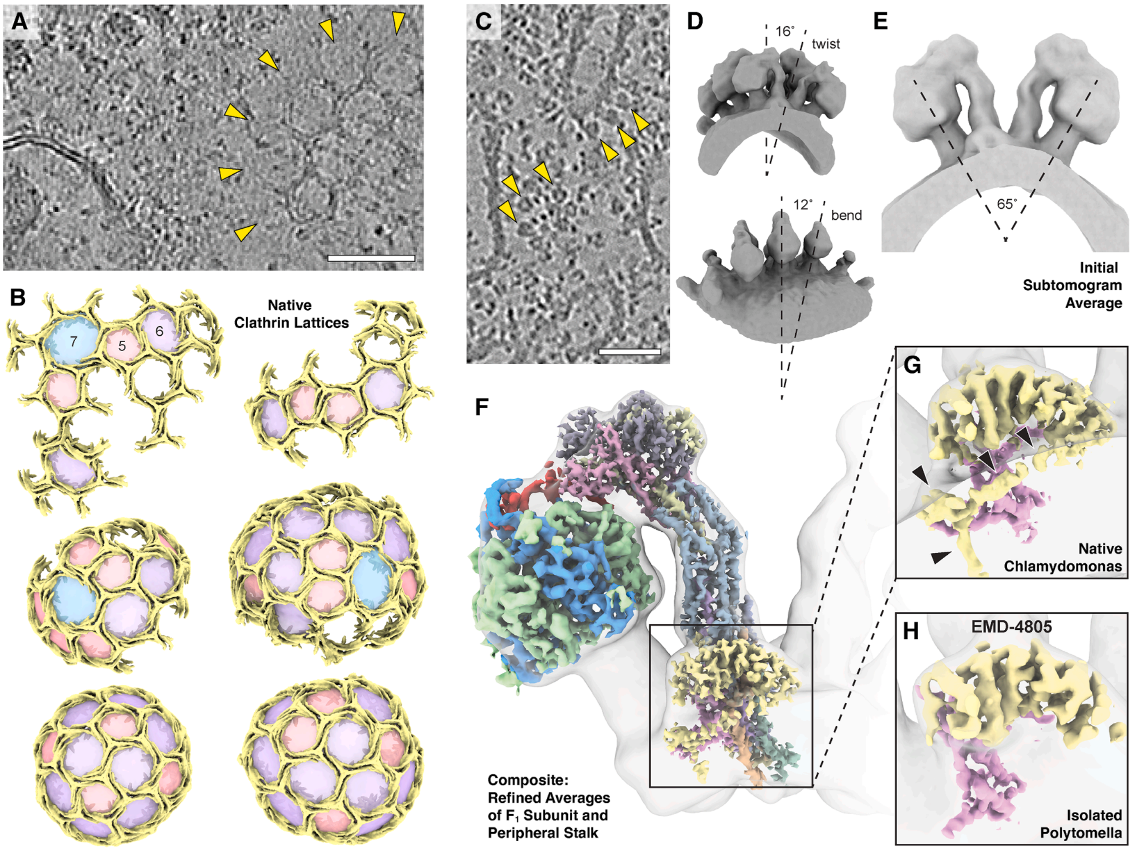

Figure 5. Structural insights into native clathrin and ATP synthase assemblies

(A) Slice through cytosol tomogram showing a clathrin coat (yellow arrowheads). Scale bar: 50 nm.

(B) Mapping clathrin structures into cellular volumes using the positions and orientations determined by STA shows how clathrin triskelia (yellow) form characteristic lattice-like coats, assembled from pentamers (5, red), hexamers (6, purple), and heptamers (7, blue). Complete polygons of the lattice have been colored to illustrate the different symmetries.

(C) Slice through a mitochondria tomogram showing cristae decorated with ATP synthase dimers (yellow arrowheads). Scale bar: 50 nm.

(D) Front and side view of ATP synthase 4× binned STA map, showing three synthase dimers forming a row. Twist (16°) and bend (12°) angles are indicated by dashed lines.

(E) Cut-through ATP synthase STA map, with a 65° angle between the two central stalks marked by dashed lines.

(F) Unbinned composite map consisting of a refined consensus map of the peripheral stalk (Figure S9N) and a refined map of a single state of the F_1 head domain (α-subunit, blue; β-subunit, light green) obtained by 3D classification (Figures S9L and S9M). This 1× binned composite map (multicolored) is shown fit within the 4× binned map from (C) (gray).

(G) Inset from (F), highlighting the a-subunit (pink) and ASA3 (yellow). Densities that have not been identified previously by single particle analysis (SPA) are indicated by black arrowheads.

(H) ASA3 (yellow) and the a-subunit (pink) of *Polytomella* sp. segmented out of the SPA map of isolated ATP synthase (EMDB: EMD-4805)[117] low-pass filtered to 5 Å. Note the differences compared with (G).

See also Figures S7 and S9.

resolving PSII, one of the most abundant membrane proteins in the chloroplast, an organelle that occupies almost half of the cell volume and accordingly constitutes a significant portion of the dataset. PSII is the starting point of the photosynthetic electron transport chain, which is responsible for converting light into biochemical energy. Functional PSII assembles into a ~600 kDa homodimeric complex, which is found in the stacked regions of the thylakoid membranes. The bulk of PSII is membrane-embedded,[118] while the luminal domains of the complex form only a small characteristic bump visible in tomograms of thylakoid membranes (Figure 4B),[90] making this a challenging test target for particle picking and STA.

Our attempts with template matching failed to accurately localize PSII (Figure S8F). Likely, strong signals arising from the membrane, as well as fringing artifacts accumulated from the repetitive architecture of stacked thylakoid membranes, interfere with obtaining clear cross-correlation peaks from template matching. To circumvent this issue, we developed a custom U-net-based picking strategy to obtain positions of 26,827 putative PSII particles from 21 high-quality chloroplast tomograms (Figures S8A–S8F). We used the defined orientation of PSII relative to the membrane to determine initial angles for the particles, followed by STA to produce a map of this membrane protein complex at a resolution of 19 Å (Figures 4B and S8G–S8J). The overall shape of our STA map agrees well with PSII models obtained by single-particle cryo-electron microscopy (cryo-EM) (Figure S8I).[118]

ATP synthase in mitochondria

Mitochondria contain several large membrane protein complexes involved in cellular energy metabolism. ATP synthase is embedded in the crista membranes, where it regenerates ATP by using the proton gradient across the membrane built up by the respiratory chain. Previous cryo-ET studies have shown that ATP synthase in yeast and animal forms rows of dimers, which induce the high membrane curvature at the crista edges.[119–121] Purified F_1F_0-ATP synthase was previously characterized by single-particle cryo-EM from a related algal species, *Polytomella* sp.[122] Recently, this line of investigation was extended with *in situ* cryo-ET to reveal ATP synthase inside native *Polytomella* cells at sub-nanometer resolution and distinguish distinct rotary conformational states of the central stalk and the F_1 head.[117]

To resolve the *in situ* structure of ATP synthase from *C. reinhardtii*, we performed template matching and STA of these large membrane complexes within native mitochondria (Figures 4F and S9). After determining an initial average of ATP synthase dimers (Figures S9A–S9K), we performed consensus refinement for the peripheral stalk region, yielding a 5.2 Å map with local resolution to 4.8 Å (Figures S9N and S9P). The F_1 head was less resolved in the consensus map due to its conformational movements. We used 3D classification to discriminate different rotary states (Figure S9L), and subsequent refinement of the most populated class yielded a map of the head region at 8.5 Å resolution (Figures S9M and S9P). While canonical ATP synthase subunits (α, β, γ, δ, ε, c10, a, and OSCP) are well conserved across species beyond *Polytomella* and *Chlamydomonas*,[123] the sturdy peripheral stalk formed by ATP-synthase-associated units (ASA1–10) is specific to these green algae species.[124] Dimers of ATP synthase are organized in helical arrays, with 13 nm spacing and 12° and 16° bend and twist angles, respectively (Figures 5C and 5D). Overall, the *in situ* structure and organization of ATP synthase are quite similar in *Chlamydomonas* and *Polytomella*. Both *in situ* structures contain extra density not present in the previous *in vitro Polytomella* structure,[122] which corresponds to the ASA3 subunit forming a long α helix parallel to the membrane and ending in a spindle-shaped density contacting the a-subunit[117] (Figures 5F–5H). However, we noted one significant difference between the *in situ* structures from these two green alga species: *Chlamydomonas* lacks the "bridge" dimer linkage between ASA1 subunits in the upper part of the peripheral stalk (Figures 4F and 5F). Interestingly, despite this difference, the angle between the two central stalks *in situ* is nearly identical in the two species (65° in *Chlamydomonas*, 66° in *Polytomella*)[117] (Figure 5E).

Data sharing and exploration for community-driven visual proteomics

EMPIAR[53] serves as the global archive for freely accessible raw electron microscopy (EM) data of biological samples. To help drive computational development and biological discovery, we have deposited both the raw and processed data corresponding to the entire 1,829 tomogram dataset into EMPIAR (32 TB in total; EMPIAR-11830). We also created a public GitHub repository with all particle positions and orientations used for the STA projects in this paper (https://github.com/Chromatin-Structure-Rhythms-Lab/ChlamyAnnotations), and we encourage future depositions by the community as additional particle classes are investigated. However, it is challenging to search and visualize large cryo-ET datasets, particularly *in situ* cellular datasets that are rich in diverse biological information. To facilitate discovery, all reconstructed tomograms have also been deposited into the CZII Cryo-ET Data Portal[54] (DS-10302), where they can be individually browsed online in a 3D volume viewer, along with annotations for particle positions and membrane surfaces (the latter generated automatically with MemBrain software).[49] We invite scientists, educators, and students to interactively explore these tomographic volumes and accompanying annotations of the native cellular environment. Additionally, this dataset serves as a learning resource, used in a recent step-by-step tutorial for processing cellular cryo-ET data, from raw frames to high-resolution subtomogram averages (https://tomoguide.github.io/).[125]

DISCUSSION

Our study demonstrates the application of modern cryo-PFIB and cryo-ET instrumentation to produce a large-scale dataset of high-quality tomograms (Figure 1), which provide a detailed view of the molecular architecture inside native *C. reinhardtii* cells (Figures 2 and 3). The complexity of biology captured in these cellular tomograms highlights the immense potential of *in situ* cryo-ET but also the significant challenges to understanding this complexity that can only be overcome through collective community efforts. We therefore provide this dataset as an open community resource, with the hope that it will enable new biological discoveries and the continued development of computational methods.

There are many biomolecular complexes awaiting structural study in this *C. reinhardtii* dataset. To verify the utility of our dataset for this purpose, we performed STA trials of seven abundant complexes (80S ribosome, Rubisco, nucleosome, MT, clathrin, PSII, and ATP synthase), which varied in size (>3 MDa to ~200 kDa) and cellular localization (Figures 1, 4, and 5). Six of these complexes reached sub-nanometer resolution, underscoring the exciting potential of modern cryo-ET workflows to resolve a variety of structures within their native cellular context. Each average was generated by a different user, each with their own STA pipeline using a distinct combination of software packages (see STAR Methods). This reflects the current state of the field, where no single standardized workflow yet suffices for robust structural and spatial analysis of all the diverse molecular targets found in cellular cryo-ET data.

Our STA trials highlight challenges that require further exploration and computational developments. In most cases, only ~20,000 particles were required to reach sub-nanometer resolution. However, in the case of small particles such as Rubisco and the nucleosome, this required classification steps that discarded 89%–94% of the particles originally selected by template matching (Figures S4C, S5C, and S5D). Template matching algorithms are less effective for detecting small particles, which provide less signal, and downstream classification routines can struggle to cleanly sort the extracted subvolumes into different class averages. This high discard rate may be partially due to biological heterogeneity: nucleosomes breathe and have many binding partners,[126–128] and pyrenoid Rubisco is bound sub-stoichiometrically by Rubisco activase and the EPYC1 linker, which a recent cryo-ET study claims causes structural heterogeneity.[101,102] However, the discard rate also reflects the inherent properties of noisy anisotropic cryo-ET data, which make it difficult to identify all true-positive instances of a target macromolecular species without also selecting false positives. These issues with template matching and classification are problematic if one wants to capture an accurate census of the macromolecules within the cellular volume, a central goal of visual proteomics. For example, while it is feasible to generate high-resolution averages of nucleosomes and Rubisco complexes through extensive classification, mapping only this small subset of true-positive particles back into the cellular volumes cannot provide accurate information about the molecular organization of chromatin or the pyrenoid matrix.

Further complicating these technical challenges is the biological challenge of the crowded native cellular environment itself. Cells present landscapes of densely packed, and even directly contacting, particles in a myriad of conformational states. Promisingly, cryo-ET method development is very active in the areas of feature detection,[48,50,129–132] particle picking,[51,133–135] and heterogeneity analysis,[68,136–138] with many new approaches leveraging neural networks. These AI-based programs benefit from large quantities of training data, which our *C. reinhardtii* dataset can help provide. Membrane proteins can be especially challenging *in situ*, exemplified by our subtomogram average of PSII. Only a relatively small portion of the protein complex extends from the density of the membrane, and the stacked thylakoid membranes themselves are exceptionally straight, resulting in strong contrast transfer function (CTF) effects that complicate particle detection and alignment. Specialized computational workflows are under development for the analysis of membranes and their embedded proteins,[49,139] including the MemBrain program, which benefited significantly from the *C. reinhardtii* dataset to improve the training of membrane segmentation.

There are numerous and varied opportunities for further biological exploration of this *C. reinhardtii* dataset.[55] Our STA trial (Figure 4A) as well as an impressive new cryo-ET study in human cells[140] showcase the potential to determine high-resolution native structures of nucleosomes, despite their small size. With 387 tomograms of the nucleus, this *C. reinhardtii* dataset provides opportunities to test the classification of nucleosomes for bound chromatin remodeling complexes and transcription factors,[141–143] as well as to search for polymerases, spliceosomes, and mRNA export complexes.[144–148] *C. reinhardtii* has proven an effective model to visualize the architecture of the nucleolus,[74] so this dataset could be used to push higher resolution native averages of pre-ribosome assembly intermediates. The nuclear periphery is well sampled in this dataset, providing opportunities to average nuclear pores,[75] which in *C. reinhardtii* are bound by proteasomes.[73] The abundant nuclear envelope and ER can enable high-resolution studies of membrane-bound ribosomes,[69] as well as cytosolic degradation microcompartments at the ER surface, which contain proteasomes and cdc48.[76] There are 246 tomograms of the Golgi, and our analysis shows the potential for high-resolution averaging of clathrin (Figure 4E). It is thus likely feasible to improve the native resolution of other coat proteins such as COPI,[78] COPII, and retromer,[79] perhaps revealing insights into cargo binding and coat assembly/disassembly. Our STA map of ATP synthase (Figure 4F) as well as a recent 5 Å map of a respiratory supercomplex[87] show the potential of resolving membrane proteins from this dataset's 581 tomograms of mitochondria. The same should be true for the 823 tomograms of the chloroplast. While PSII remains a challenge that requires further development (Figure 4B), another promising candidate is the TIC/TOC translocon in the chloroplast envelope, which was recently resolved by cryo-EM of isolated complexes[149,150] and awaits study within the cellular environment. Of course, beyond the analysis of these well-known macromolecules, this large-scale *C. reinhardtii* dataset also offers opportunities to discover native complexes and higher-order assemblies that have so far eluded characterization. With sufficiently accurate annotation of complexes, the molecular organization revealed in these tomograms may also be used to build molecular simulations of cellular compartments,[2,140,151,152] such as crista or thylakoid membranes as well as Rubisco or chromatin condensates.

To realize the goals of visual proteomics, cryo-ET analysis must dig deeper to resolve the rich diversity of molecular complexes inside cells. Especially for less abundant complexes, this goal would strongly benefit from large repositories of publicly available high-quality data that are easy to search, explore, and combine. *In situ* cryo-ET datasets are dense with information that has uses well beyond the specific aims of a single study or research group. The challenge is to establish best practices and new tools that will unlock the value of all that unused visual proteomics information. Continued efforts to facilitate the process of data sharing within the cryo-ET community can help bring about the next generation of AI-driven computational methods. Combined with parallel advancements in mass spectrometry and structure prediction,[2] these methods may be able to provide deep inventories of diverse biomolecular complexes in tomograms, revealing their structures, their conformational heterogeneity, their interactions, and their 3D molecular organization inside native cells.

Limitations of the study

The *C. reinhardtii* cells used for this study were grown in asynchronous culture under mixotrophic conditions (combination of heterotrophy and autotrophy) without controlling specific physiological factors. As a result, the data are not representative of a particular metabolic or photosynthetic state nor a specific cell cycle stage. Regions of interest were chosen for tomogram acquisition in a user-guided fashion, targeting specific organelles of interest (e.g., mitochondria, chloroplast, Golgi, and nuclear periphery). Thus, although this large-scale dataset fairly comprehensively captures the internal features of *C. reinhardtii* cells, certain organelles are more represented than others. Several different computational workflows were used for particle picking and STA of the different molecular complexes examined here. While this mirrors how the dataset will likely be used by the global community, it is not the intention of this study to quantitatively compare different software packages for cryo-ET analysis. To assess the quality of our dataset, we focused on known abundant complexes of different sizes. In several cases, the majority of detected particles were discarded in order to reach a more homogeneous high-resolution class average. There is substantial conformational and compositional heterogeneity in these native complexes that remains to be studied, including binding of linker proteins and cofactors to Rubisco, structural changes in nucleosomes upon binding of transcription factors and remodelers, assembly of clathrin intermediate structures, and the extensive motion of ATP synthase throughout its catalytic cycle. Most promisingly, there are many unknown complexes visualized in these native views of the cellular environment, which we intentionally did not average but rather left for the community to investigate in biological studies.

RESOURCE AVAILABILITY

Lead contact

Requests for further information and resources should be directed to and will be fulfilled by the lead contact, Benjamin D. Engel (ben.engel@unibas.ch).

Materials availability

This study did not generate new, unique reagents.

Data and code availability

- Raw EM data are available at the EMPIAR under accession code EMPIAR: EMPIAR-11830. Annotation and processing information for all 1,829 tomograms are provided in spreadsheet format.[153] The following subtomogram averages have been deposited at the Electron Microscopy Data Bank (EMDB): 80S ribosome (EMDB: EMD-51847), nucleosome (EMDB: EMD-19906), PSII (EMDB: EMD-51731), Rubisco (EMDB: EMD-51848), microtubule (EMDB: EMD-51804), clathrin (EMDB: EMD-51789), and ATP synthase (EMDB: EMD-51802). Segmentations shown in Figures 2 and 3 are deposited on Zenodo (https://doi.org/10.5281/zenodo.15875785). Particle positions and orientations used for STA, along with all resources derived from this work, are available on GitHub (https://github.com/Chromatin-Structure-Rhythms-Lab/ChlamyAnnotations). Reconstructed tomograms and annotations are also available to explore interactively at the CZII Cryo-ET Data Portal (DS-10302, https://cryoetdataportal.czscience.com/datasets/10302/). Raw data for cryo-PFIB/SEM slice-and-view of a whole *C. reinhardtii* cell has also been deposited (EMPIAR: EMPIAR-11275).
- This paper does not report original code.
- Any additional information required to reanalyze the data reported in this paper is available from the lead contact upon request.

ACKNOWLEDGMENTS

Calculations were performed at the Max Planck Institute of Biochemistry and the Raven Supercomputer of the Max Planck Computing and Data Facility (MPCDF) in Garching, Germany; at the sciCORE (http://scicore.unibas.ch/) scientific computing center at the University of Basel, Switzerland; and at Thermo Fisher Scientific, in Eindhoven, the Netherlands. This work was supported by Thermo Fisher Scientific. All lamella preparations and tilt-series collections used in this work were conducted at Thermo Fisher R&D facilities in Brno and Eindhoven, utilizing Arctis and Krios microscopes. This work was also supported by the ERC consolidator grant "cryOcean" (fulfilled by the Swiss State Secretariat for Education, Research and Innovation, M822.00045) as well as a Swiss Nanoscience Institute PhD school grant to B.D.E. and P.V.d.S., an EMBO long-term postdoctoral fellowship (ALTF-383-2022) to G.T., an SNSF Postdoctoral Fellowship (project 210561) to F.W., a Boehringer Ingelheim Fonds fellowship to L.L., and by the Max Planck Society to J.A.G.B. and J.M.P.

AUTHOR CONTRIBUTIONS

Cell growth and vitrification were done by W. Wietrzynski, S.K., F.W., C.L.M., and S.v.D.; FIB milling was done by R.K., X.Z., and A.K.; tilt-series acquisition was done by X.Z., M.O., and A.K.; data preprocessing and reconstruction were done by S.K. and R.D.R. with support from W. Wan; data cleaning, curation, and annotation were done by S.K., R.D.R., A.K.M., S.v.D., F.W., C.L.M., P.V.d.S., H.v.d.H., and W. Wietrzynski; and volume segmentation was done by J.H., M.O., L.L., and S.Z. STA was done by S.K. (ribosome and Rubisco); M.O., S.K., and F.W. (ATP synthase); S.C. and M.O. (MT); G.T. (clathrin); A.K.M., M.O., and R.D.R. (nucleosome); and S.v.D., R.D.R., J.H., and L.L. (PSII). Curation of particle positions on GitHub was done by P.H.; creation of the TomoGuide tutorial was done by P.V.d.S. and F.W.; figure composition was done by S.K., R.D.R., J.H., M.O., S.C., S.K., G.T., A.K.M., S.v.D., A.K., and B.D.E.; manuscript writing and editing were led by B.D.E. and A.K. with support from J.H. and contributions from all authors; and supervision was done by J.A.G.B., J.M.P., B.D.E., and A.K.

DECLARATION OF INTERESTS

R.K., S.K., M.O., J.H., X.J., S.C., and A.K. were employees of Thermo Fisher Scientific while working on this project.

STAR★METHODS

Detailed methods are provided in the online version of this paper and include the following:

SUPPLEMENTAL INFORMATION

Supplemental information can be found online at https://doi.org/10.1016/j.molcel.2025.11.029.

Received: January 8, 2025
Revised: October 24, 2025
Accepted: November 26, 2025
Published: December 19, 2025

REFERENCES

1. Nickell, S., Kofler, C., Leis, A.P., and Baumeister, W. (2006). A visual approach to proteomics. Nat. Rev. Mol. Cell Biol. *7*, 225–230. https://doi.org/10.1038/nrm1861.
2. McCafferty, C.L., Klumpe, S., Amaro, R.E., Kukulski, W., Collinson, L., and Engel, B.D. (2024). Integrating cellular electron microscopy with multimodal data to explore biology across space and time. Cell *187*, 563–584. https://doi.org/10.1016/j.cell.2024.01.005.
3. Young, L.N., and Villa, E. (2023). Bringing Structure to Cell Biology with Cryo-Electron Tomography. Annu. Rev. Biophys. *52*, 573–595. https://doi.org/10.1146/annurev-biophys-111622-091327.
4. Nogales, E., and Mahamid, J. (2024). Bridging structural and cell biology with cryo-electron microscopy. Nature *628*, 47–56. https://doi.org/10.1038/s41586-024-07198-2.
5. Ferreira, J.L., Pražák, V., Vasishtan, D., Siggel, M., Hentzschel, F., Binder, A.M., Pietsch, E., Kosinski, J., Frischknecht, F., Gilberger, T.W., et al. (2023). Variable microtubule architecture in the malaria parasite. Nat. Commun. *14*, 1216. https://doi.org/10.1038/s41467-023-36627-5.
6. Rodrigues-Oliveira, T., Wollweber, F., Ponce-Toledo, R.I., Xu, J., Rittmann, S.K.R., Klingl, A., Pilhofer, M., and Schleper, C. (2023). Actin cytoskeleton and complex cell architecture in an Asgard archaeon. Nature *613*, 332–339. https://doi.org/10.1038/s41586-022-05550-y.
7. Dietrich, H.M., Righetto, R.D., Kumar, A., Wietrzynski, W., Trischler, R., Schuller, S.K., Wagner, J., Schwarz, F.M., Engel, B.D., Müller, V., et al. (2022). Membrane-anchored HDCR nanowires drive hydrogen-powered CO2 fixation. Nature *607*, 823–830. https://doi.org/10.1038/s41586-022-04971-z.
8. Jasnin, M., Beck, F., Ecke, M., Fukuda, Y., Martinez-Sanchez, A., Baumeister, W., and Gerisch, G. (2019). The Architecture of Traveling Actin Waves Revealed by Cryo-Electron Tomography. Structure *27*, 1211–1223.e5. https://doi.org/10.1016/j.str.2019.05.009.
9. Zimmerli, C.E., Allegretti, M., Rantos, V., Goetz, S.K., Obarska-Kosinska, A., Zagoriy, I., Halavatyi, A., Hummer, G., Mahamid, J., Kosinski, J., et al. (2021). Nuclear pores dilate and constrict in cellulo. Science *374*, eabd9776. https://doi.org/10.1126/science.abd9776.
10. Tamborrini, D., Wang, Z., Wagner, T., Tacke, S., Stabrin, M., Grange, M., Kho, A.L., Rees, M., Bennett, P., Gautel, M., et al. (2023). Structure of the native myosin filament in the relaxed cardiac sarcomere. Nature *623*, 863–871. https://doi.org/10.1038/s41586-023-06690-5.
11. Pöge, M., Mahamid, J., Imanishi, S.S., Plitzko, J.M., Palczewski, K., and Baumeister, W. (2021). Determinants shaping the nanoscale architecture of the mouse rod outer segment. eLife *10*, e72817. https://doi.org/10.7554/eLife.72817.
12. Laughlin, T.G., Deep, A., Prichard, A.M., Seitz, C., Gu, Y., Enustun, E., Suslov, S., Khanna, K., Birkholz, E.A., Armbruster, E., et al. (2022). Architecture and self-assembly of the jumbo bacteriophage nuclear shell. Nature *608*, 429–435. https://doi.org/10.1038/s41586-022-05013-4.
13. Schiøtz, O.H., Kaiser, C.J.O., Klumpe, S., Morado, D.R., Poege, M., Schneider, J., Beck, F., Klebl, D.P., Thompson, C., and Plitzko, J.M. (2023). Serial Lift-Out: sampling the molecular anatomy of whole organisms. Nat. Methods *21*, 1684–1692. https://doi.org/10.1038/s41592-023-02113-5.
14. Zens, B., Fäßler, F., Hansen, J.M., Hauschild, R., Datler, J., Hodirnau, V.-V., Zheden, V., Alanko, J., Sixt, M., and Schur, F.K.M. (2024). Lift-out cryo-FIBSEM and cryo-ET reveal the ultrastructural landscape of extracellular matrix. J. Cell Biol. *223*, e202309125. https://doi.org/10.1083/jcb.202309125.
15. Creekmore, B.C., Kixmoeller, K., Black, B.E., Lee, E.B., and Chang, Y.-W. (2024). Ultrastructure of human brain tissue vitrified from autopsy revealed by cryo-ET with cryo-plasma FIB milling. Nat. Commun. *15*, 2660. https://doi.org/10.1038/s41467-024-47066-1.
16. Klumpe, S., Fung, H.K., Goetz, S.K., Zagoriy, I., Hampoelz, B., Zhang, X., Erdmann, P.S., Baumbach, J., Müller, C.W., Beck, M., et al. (2021). A modular platform for automated cryo-FIB workflows. eLife *10*, e70506. https://doi.org/10.7554/eLife.70506.
17. Cleeve, P., Dierickx, D., Naegele, L., Kannachel, R., Burne, L., Buckley, G., Gorelick, S., Whisstock, J.C., and de Marco, A. (2023). OpenFIBSEM: A universal API for FIBSEM control. J. Struct. Biol. *215*, 107967. https://doi.org/10.1016/j.jsb.2023.107967.
18. Zachs, T., Schertel, A., Medeiros, J., Weiss, G.L., Hugener, J., Matos, J., and Pilhofer, M. (2020). Fully automated, sequential focused ion beam milling for cryo-electron tomography. eLife *9*, e52286. https://doi.org/10.7554/eLife.52286.
19. Tacke, S., Erdmann, P., Wang, Z., Klumpe, S., Grange, M., Plitzko, J., and Raunser, S. (2021). A streamlined workflow for automated cryo focused ion beam milling. J. Struct. Biol. *213*, 107743. https://doi.org/10.1016/j.jsb.2021.107743.
20. Khavnekar, S., Wan, W., Majumder, P., Wietrzynski, W., Erdmann, P.S., and Plitzko, J.M. (2023). Multishot tomography for high-resolution in situ subtomogram averaging. J. Struct. Biol. *215*, 107911. https://doi.org/10.1016/j.jsb.2022.107911.
21. Bouvette, J., Liu, H.-F., Du, X., Zhou, Y., Sikkema, A.P., da Fonseca Rezende E Mello, J., Klemm, B.P., Huang, R., Schaaper, R.M., Borgnia, M.J., et al. (2021). Beam image-shift accelerated data acquisition for near-atomic resolution single-particle cryo-electron tomography. Nat. Commun. *12*, 1957. https://doi.org/10.1038/s41467-021-22251-8.
22. Eisenstein, F., Yanagisawa, H., Kashihara, H., Kikkawa, M., Tsukita, S., and Danev, R. (2023). Parallel cryo electron tomography on in situ lamellae. Nat. Methods *20*, 131–138. https://doi.org/10.1038/s41592-022-01690-1.
23. Eisenstein, F., Fukuda, Y., and Danev, R. (2024). Smart parallel automated cryo-electron tomography. Nat. Methods *21*, 1612–1615. https://doi.org/10.1038/s41592-024-02373-9.
24. Yang, J.E., Larson, M.R., Sibert, B.S., Kim, J.Y., Parrell, D., Sanchez, J.C., Pappas, V., Kumar, A., Cai, K., Thompson, K., et al. (2023). Correlative montage parallel array cryo-tomography for in situ structural cell biology. Nat. Methods *20*, 1537–1543. https://doi.org/10.1038/s41592-023-01999-5.
25. Berger, C., Dumoux, M., Glen, T., Yee, N.B.-Y., Mitchels, J.M., Patáková, Z., Darrow, M.C., Naismith, J.H., and Grange, M. (2023). Plasma FIB milling for the determination of structures in situ. Nat. Commun. *14*, 629. https://doi.org/10.1038/s41467-023-36372-9.
26. Cruz-León, S., Majtner, T., Hoffmann, P.C., Kreysing, J.P., Kehl, S., Tuijtel, M.W., Schaefer, S.L., Geißler, K., Beck, M., Turoňová, B., et al. (2024). High-confidence 3D template matching for cryo-electron tomography. Nat. Commun. *15*, 3992. https://doi.org/10.1038/s41467-024-47839-8.
27. Lucas, B.A., Himes, B.A., and Grigorieff, N. (2023). Baited reconstruction with 2D template matching for high-resolution structure determination in vitro and in vivo without template bias. eLife *12*, RP90486. https://doi.org/10.7554/eLife.90486.
28. Wan, W., Khavnekar, S., and Wagner, J. (2024). STOPGAP: an open-source package for template matching, subtomogram alignment and classification. Acta Crystallogr. D Struct. Biol. *80*, 336–349. https://doi.org/10.1107/S205979832400295X.
29. Hrabe, T., Chen, Y., Pfeffer, S., Cuellar, L.K., Mangold, A.-V., and Förster, F. (2012). PyTom: a python-based toolbox for localization of macromolecules in cryo-electron tomograms and subtomogram analysis. J. Struct. Biol. *178*, 177–188. https://doi.org/10.1016/j.jsb.2011.12.003.
30. Chaillet, M.L., van der Schot, G., Gubins, I., Roet, S., Veltkamp, R.C., and Förster, F. (2023). Extensive Angular Sampling Enables the Sensitive Localization of Macromolecules in Electron Tomograms. Int. J. Mol. Sci. *24*, 13375. https://doi.org/10.3390/ijms241713375.

31. Tegunov, D., Xue, L., Dienemann, C., Cramer, P., and Mahamid, J. (2021). Multi-particle cryo-EM refinement with M visualizes ribosome-antibiotic complex at 3.5 Å in cells. Nat. Methods *18*, 186–193. https://doi.org/10.1038/s41592-020-01054-7.

32. Burt, A., Toader, B., Warshamanage, R., von Kügelgen, A., Pyle, E., Zivanov, J., Kimanius, D., Bharat, T.A.M., and Scheres, S.H.W. (2024). An image processing pipeline for electron cryo-tomography in RELION-5. FEBS Open Bio *14*, 1788–1804. https://doi.org/10.1002/2211-5463.13873.

33. Balyschew, N., Yushkevich, A., Mikirtumov, V., Sanchez, R.M., Sprink, T., and Kudryashev, M. (2023). Streamlined structure determination by cryo-electron tomography and subtomogram averaging using TomoBEAR. Nat. Commun. *14*, 6543. https://doi.org/10.1038/s41467-023-42085-w.

34. Chen, M., Bell, J.M., Shi, X., Sun, S.Y., Wang, Z., and Ludtke, S.J. (2019). A complete data processing workflow for cryo-ET and subtomogram averaging. Nat. Methods *16*, 1161–1168. https://doi.org/10.1038/s41592-019-0591-8.

35. Liu, H.-F., Zhou, Y., Huang, Q., Piland, J., Jin, W., Mandel, J., Du, X., Martin, J., and Bartesaghi, A. (2023). nextPYP: a comprehensive and scalable platform for characterizing protein variability in situ using single-particle cryo-electron tomography. Nat. Methods *20*, 1909–1919. https://doi.org/10.1038/s41592-023-02045-0.

36. Castaño-Díez, D., Kudryashev, M., Arheit, M., and Stahlberg, H. (2012). Dynamo: a flexible, user-friendly development tool for subtomogram averaging of cryo-EM data in high-performance computing environments. J. Struct. Biol. *178*, 139–151. https://doi.org/10.1016/j.jsb.2011.12.017.

37. Himes, B.A., and Zhang, P. (2018). emClarity: software for high-resolution cryo-electron tomography and subtomogram averaging. Nat. Methods *15*, 955–961. https://doi.org/10.1038/s41592-018-0167-z.

38. Fäßler, F., Dimchev, G., Hodirnau, V.-V., Wan, W., and Schur, F.K.M. (2020). Cryo-electron tomography structure of Arp2/3 complex in cells reveals new insights into the branch junction. Nat. Commun. *11*, 6437. https://doi.org/10.1038/s41467-020-20286-x.

39. Zhang, X., Sridharan, S., Zagoriy, I., Eugster Oegema, C., Ching, C., Pflaesterer, T., Fung, H.K.H., Becher, I., Poser, I., Müller, C.W., et al. (2023). Molecular mechanisms of stress-induced reactivation in mumps virus condensates. Cell *186*, 1877–1894.e27. https://doi.org/10.1016/j.cell.2023.03.015.

40. Sutton, G., Sun, D., Fu, X., Kotecha, A., Hecksel, C.W., Clare, D.K., Zhang, P., Stuart, D.I., and Boyce, M. (2020). Assembly intermediates of orthoreovirus captured in the cell. Nat. Commun. *11*, 4445. https://doi.org/10.1038/s41467-020-18243-9.

41. Wang, Z., Grange, M., Pospich, S., Wagner, T., Kho, A.L., Gautel, M., and Raunser, S. (2022). Structures from intact myofibrils reveal mechanism of thin filament regulation through nebulin. Science *375*, eabn1934. https://doi.org/10.1126/science.abn1934.

42. Xue, L., Lenz, S., Zimmermann-Kogadeeva, M., Tegunov, D., Cramer, P., Bork, P., Rappsilber, J., and Mahamid, J. (2022). Visualizing translation dynamics at atomic detail inside a bacterial cell. Nature *610*, 205–211. https://doi.org/10.1038/s41586-022-05255-2.

43. Xing, H., Taniguchi, R., Khusainov, I., Kreysing, J.P., Welsch, S., Turoňová, B., and Beck, M. (2023). Translation dynamics in human cells visualized at high resolution reveal cancer drug action. Science *381*, 70–75. https://doi.org/10.1126/science.adh1411.

44. Hoffmann, P.C., Kreysing, J.P., Khusainov, I., Tuijtel, M.W., Welsch, S., and Beck, M. (2022). Structures of the eukaryotic ribosome and its translational states in situ. Nat. Commun. *13*, 7435. https://doi.org/10.1038/s41467-022-34997-w.

45. Anton, L., Cheng, W., Haile, M.T., Cobb, D.W., Zhu, X., Han, L., Li, E., Nair, A., Lee, C.L., Ke, H., et al. (2023). Multiscale effects of perturbed translation dynamics inform antimalarial design. Nat. Struct. Mol. Biol. *32*, 2158–2164. https://doi.org/10.1101/2023.09.03.556115.

46. Zheng, W., Zhang, Y., Wang, J., Wang, S., Chai, P., Bailey, E.J., Guo, W., Devarkar, S.C., Wu, S., Lin, J., et al. (2024). Visualizing the translation landscape in human cells at high resolution. Preprint at bioRxiv. https://doi.org/10.1101/2024.07.02.601723.

47. Rickgauer, J.P., Choi, H., Moore, A.S., Denk, W., and Lippincott-Schwartz, J. (2024). Structural dynamics of human ribosomes in situ reconstructed by exhaustive high-resolution template matching. Mol. Cell *84*, 4912–4928.e7. https://doi.org/10.1016/j.molcel.2024.11.003.

48. Rice, G., Wagner, T., Stabrin, M., Sitsel, O., Prumbaum, D., and Raunser, S. (2023). TomoTwin: generalized 3D localization of macromolecules in cryo-electron tomograms with structural data mining. Nat. Methods *20*, 871–880. https://doi.org/10.1038/s41592-023-01878-z.

49. Lamm, L., Zufferey, S., Zhang, H., Righetto, R.D., Waltz, F., Wietrzynski, W., Yamauchi, K.A., Burt, A., Liu, Y., Martinez-Sanchez, A., et al. (2024). MemBrain v2: an end-to-end tool for the analysis of membranes in cryo-electron tomography. Preprint at bioRxiv. https://doi.org/10.1101/2024.01.05.574336.

50. de Teresa-Trueba, I., Goetz, S.K., Mattausch, A., Stojanovska, F., Zimmerli, C.E., Toro-Nahuelpan, M., Cheng, D.W.C., Tollervey, F., Pape, C., Beck, M., et al. (2023). Convolutional networks for supervised mining of molecular patterns within cellular context. Nat. Methods *20*, 284–294. https://doi.org/10.1038/s41592-022-01746-2.

51. Moebel, E., Martinez-Sanchez, A., Lamm, L., Righetto, R.D., Wietrzynski, W., Albert, S., Larivière, D., Fourmentin, E., Pfeffer, S., Ortiz, J., et al. (2021). Deep learning improves macromolecule identification in 3D cellular cryo-electron tomograms. Nat. Methods *18*, 1386–1394. https://doi.org/10.1038/s41592-021-01275-4.

52. Chen, M., Dai, W., Sun, S.Y., Jonasch, D., He, C.Y., Schmid, M.F., Chiu, W., and Ludtke, S.J. (2017). Convolutional neural networks for automated annotation of cellular cryo-electron tomograms. Nat. Methods *14*, 983–985. https://doi.org/10.1038/nmeth.4405.

53. Iudin, A., Korir, P.K., Somasundharam, S., Weyand, S., Cattavitello, C., Fonseca, N., Salih, O., Kleywegt, G.J., and Patwardhan, A. (2023). EMPIAR: the Electron Microscopy Public Image Archive. Nucleic Acids Res. *51*, D1503–D1511. https://doi.org/10.1093/nar/gkac1062.

54. Ermel, U., Cheng, A., Ni, J.X., Gadling, J., Venkatakrishnan, M., Evans, K., Asuncion, J., Sweet, A., Pourroy, J., Wang, Z.S., et al. (2024). A data portal for providing standardized annotations for cryo-electron tomography. Nat. Methods *21*, 2200–2202. https://doi.org/10.1038/s41592-024-02477-2.

55. Goodenough, U., and Engel, B.D. (2023). Cell ultrastructure. Chapter 2. In The Chlamydomonas Sourcebook, Third Edition, U. Goodenough, ed. (Academic Press), pp. 17–40. https://doi.org/10.1016/B978-0-12-822457-1.00015-7.

56. Jinkerson, R.E., and Jonikas, M.C. (2015). Molecular techniques to interrogate and edit the Chlamydomonas nuclear genome. Plant J. *82*, 393–412. https://doi.org/10.1111/tpj.12801.

57. Crozet, P., Navarro, F.J., Willmund, F., Mehrshahi, P., Bakowski, K., Lauersen, K.J., Pérez-Pérez, M.-E., Auroy, P., Gorchs Rovira, A., Sauret-Gueto, S., et al. (2018). Birth of a Photosynthetic Chassis: A MoClo Toolkit Enabling Synthetic Biology in the Microalga Chlamydomonas reinhardtii. ACS Synth. Biol. *7*, 2074–2086. https://doi.org/10.1021/acssynbio.8b00251.

58. Salomé, P.A., and Merchant, S.S. (2019). A Series of Fortunate Events: Introducing Chlamydomonas as a Reference Organism. Plant Cell *31*, 1682–1707. https://doi.org/10.1105/tpc.18.00952.

59. Sasso, S., Stibor, H., Mittag, M., and Grossman, A.R. (2018). From molecular manipulation of domesticated Chlamydomonas reinhardtii to survival in nature. eLife *7*, e39233. https://doi.org/10.7554/eLife.39233.

60. Marshall, W.F. (2024). Chlamydomonas as a model system to study cilia and flagella using genetics, biochemistry, and microscopy. Front. Cell Dev. Biol. *12*, 1412641. https://doi.org/10.3389/fcell.2024.1412641.

61. Sergey, G., Denis, K., Ava, H., Gediminas, G., Viola, O., Kaluza, O.L., Law, R.H.P., O'Bryan, M., Roger, P., James, C.W., et al. (2018). Oxygen plasma focused ion beam scanning electron microscopy for biological samples. Preprint at bioRxiv. https://doi.org/10.1101/457820.
62. Kuba, J., Mitchels, J., Hovorka, M., Erdmann, P., Berka, L., Kirmse, R., König, J., DE Bock, J., Goetze, B., and Rigort, A. (2021). Advanced cryo-tomography workflow developments - correlative microscopy, milling automation and cryo-lift-out. J. Microsc. *281*, 112–124. https://doi.org/10.1111/jmi.12939.
63. Brogden, V., Johnson, C., Rue, C., Graham, J., Langworthy, K., Golledge, S., and McMorran, B. (2021). Material Sputtering with a Multi-Ion Species Plasma Focused Ion Beam. Adv. Mater. Sci. Eng. *2021*, 1–9. https://doi.org/10.1155/2021/8842777.
64. Dumoux, M., Glen, T., Smith, J.L.R., Ho, E.M.L., Perdigão, L.M.A., Pennington, A., Klumpe, S., Yee, N.B.Y., Farmer, D.A., Lai, P.Y.A., et al. (2023). Cryo-plasma FIB/SEM volume imaging of biological specimens. eLife *12*, e83623. https://doi.org/10.7554/eLife.83623.
65. Berger, C., Watson, H., Naismith, J., Dumoux, M., and Grange, M. (2025). Xenon plasma focused ion beam lamella fabrication on high-pressure frozen specimens for structural cell biology. Nat. Commun. *16*, 2286. https://doi.org/10.1038/s41467-025-57493-3.
66. Spurný, R., Patáková, Z., Dolník, M., Kříž, R., Mitchels, J., Rigort, A., and Hovorka, M. (2023). Arctis WebUI - A Novel Software Concept for Automating Cryo-lamellae Production. Microsc. Microanal. *29*, 2081–2082. https://doi.org/10.1093/micmic/ozad067.1077.
67. Buchholz, T.-O., Jordan, M., Pigino, G., and Jug, F. (2019). Cryo-CARE: Content-aware image restoration for cryo-transmission electron microscopy data. In 2019 IEEE 16th International Symposium on Biomedical Imaging (ISBI 2019) (IEEE). https://doi.org/10.1109/isbi.2019.8759519.
68. Rangan, R., Feathers, R., Khavnekar, S., Lerer, A., Johnston, J.D., Kelley, R., Obr, M., Kotecha, A., and Zhong, E.D. (2024). CryoDRGN-ET: deep reconstructing generative networks for visualizing dynamic biomolecules inside cells. Nat. Methods *21*, 1537–1545. https://doi.org/10.1038/s41592-024-02340-4.
69. Pfeffer, S., Dudek, J., Schaffer, M., Ng, B.G., Albert, S., Plitzko, J.M., Baumeister, W., Zimmermann, R., Freeze, H.H., Engel, B.D., et al. (2017). Dissecting the molecular organization of the translocon-associated protein complex. Nat. Commun. *8*, 14516. https://doi.org/10.1038/ncomms14516.
70. Tuijtel, M.W., Cruz-León, S., Kreysing, J.P., Welsch, S., Hummer, G., Beck, M., and Turoňová, B. (2024). Thinner is not always better: Optimizing cryo-lamellae for subtomogram averaging. Sci. Adv. *10*, eadk6285. https://doi.org/10.1126/sciadv.adk6285.
71. Lucas, B.A., and Grigorieff, N. (2023). Quantification of gallium cryo-FIB milling damage in biological lamellae. Proc. Natl. Acad. Sci. USA *120*, e2301852120. https://doi.org/10.1073/pnas.2301852120.
72. Rosenthal, P.B., and Henderson, R. (2003). Optimal Determination of Particle Orientation, Absolute Hand, and Contrast Loss in Single-particle Electron Cryomicroscopy. J. Mol. Biol. *333*, 721–745. https://doi.org/10.1016/j.jmb.2003.07.013.
73. Albert, S., Schaffer, M., Beck, F., Mosalaganti, S., Asano, S., Thomas, H.F., Plitzko, J.M., Beck, M., Baumeister, W., and Engel, B.D. (2017). Proteasomes tether to two distinct sites at the nuclear pore complex. Proc. Natl. Acad. Sci. USA *114*, 13726–13731. https://doi.org/10.1073/pnas.1716305114.
74. Erdmann, P.S., Hou, Z., Klumpe, S., Khavnekar, S., Beck, F., Wilfling, F., Plitzko, J.M., and Baumeister, W. (2021). In situ cryo-electron tomography reveals gradient organization of ribosome biogenesis in intact nucleoli. Nat. Commun. *12*, 5364. https://doi.org/10.1038/s41467-021-25413-w.
75. Mosalaganti, S., Kosinski, J., Albert, S., Schaffer, M., Strenkert, D., Salomé, P.A., Merchant, S.S., Plitzko, J.M., Baumeister, W., Engel, B.D., et al. (2018). In situ architecture of the algal nuclear pore complex. Nat. Commun. *9*, 2361. https://doi.org/10.1038/s41467-018-04739-y.
76. Albert, S., Wietrzynski, W., Lee, C.-W., Schaffer, M., Beck, F., Schuller, J.M., Salomé, P.A., Plitzko, J.M., Baumeister, W., and Engel, B.D. (2020). Direct visualization of degradation microcompartments at the ER membrane. Proc. Natl. Acad. Sci. USA *117*, 1069–1080. https://doi.org/10.1073/pnas.1905641117.
77. Engel, B.D., Schaffer, M., Albert, S., Asano, S., Plitzko, J.M., and Baumeister, W. (2015). In situ structural analysis of Golgi intracisternal protein arrays. Proc. Natl. Acad. Sci. USA *112*, 11264–11269. https://doi.org/10.1073/pnas.1515337112.
78. Bykov, Y.S., Schaffer, M., Dodonova, S.O., Albert, S., Plitzko, J.M., Baumeister, W., Engel, B.D., and Briggs, J.A. (2017). The structure of the COPI coat determined within the cell. eLife *6*, e32493. https://doi.org/10.7554/eLife.32493.
79. Kovtun, O., Leneva, N., Bykov, Y.S., Ariotti, N., Teasdale, R.D., Schaffer, M., Engel, B.D., Owen, D.J., Briggs, J.A.G., and Collins, B.M. (2018). Structure of the membrane-assembled retromer coat determined by cryo-electron tomography. Nature *561*, 561–564. https://doi.org/10.1038/s41586-018-0526-z.
80. Le Guennec, M., Klena, N., Gambarotto, D., Laporte, M.H., Tassin, A.-M., van den Hoek, H., Erdmann, P.S., Schaffer, M., Kovacik, L., Borgers, S., et al. (2020). A helical inner scaffold provides a structural basis for centriole cohesion. Sci. Adv. *6*, eaaz4137. https://doi.org/10.1126/sciadv.aaz4137.
81. Klena, N., Le Guennec, M., Tassin, A.-M., van den Hoek, H., Erdmann, P.S., Schaffer, M., Geimer, S., Aeschlimann, G., Kovacik, L., Sadian, Y., et al. (2020). Architecture of the centriole cartwheel-containing region revealed by cryo-electron tomography. EMBO J. *39*, e106246. https://doi.org/10.15252/embj.2020106246.
82. van den Hoek, H., Klena, N., Jordan, M.A., Alvarez Viar, G., Righetto, R.D., Schaffer, M., Erdmann, P.S., Wan, W., Geimer, S., Plitzko, J.M., et al. (2022). In situ architecture of the ciliary base reveals the stepwise assembly of intraflagellar transport trains. Science *377*, 543–548. https://doi.org/10.1126/science.abm6704.
83. Jordan, M.A., Diener, D.R., Stepanek, L., and Pigino, G. (2018). The cryo-EM structure of intraflagellar transport trains reveals how dynein is inactivated to ensure unidirectional anterograde movement in cilia. Nat. Cell Biol. *20*, 1250–1255. https://doi.org/10.1038/s41556-018-0213-1.
84. Lacey, S.E., Foster, H.E., and Pigino, G. (2023). The molecular structure of IFT-A and IFT-B in anterograde intraflagellar transport trains. Nat. Struct. Mol. Biol. *30*, 584–593. https://doi.org/10.1038/s41594-022-00905-5.
85. Craig, E.W., Mueller, D.M., Bigge, B.M., Schaffer, M., Engel, B.D., and Avasthi, P. (2019). The elusive actin cytoskeleton of a green alga expressing both conventional and divergent actins. Mol. Biol. Cell *30*, 2827–2837. https://doi.org/10.1091/mbc.E19-03-0141.
86. Waltz, F., Salinas-Giegé, T., Englmeier, R., Meichel, H., Soufari, H., Kuhn, L., Pfeffer, S., Förster, F., Engel, B.D., Giegé, P., et al. (2021). How to build a ribosome from RNA fragments in Chlamydomonas mitochondria. Nat. Commun. *12*, 7176. https://doi.org/10.1038/s41467-021-27200-z.
87. Waltz, F., Righetto, R.D., Lamm, L., Salinas-Giegé, T., Kelley, R., Zhang, X., Obr, M., Khavnekar, S., Kotecha, A., and Engel, B.D. (2025). In-cell architecture of the mitochondrial respiratory chain. Science *387*, 1296–1301. https://doi.org/10.1126/science.ads8738.
88. Engel, B.D., Schaffer, M., Kuhn Cuellar, L., Villa, E., Plitzko, J.M., and Baumeister, W. (2015). Native architecture of the Chlamydomonas chloroplast revealed by in situ cryo-electron tomography. eLife *4*, e04889. https://doi.org/10.7554/eLife.04889.
89. Freeman Rosenzweig, E.S., Xu, B., Kuhn Cuellar, L., Martinez-Sanchez, A., Schaffer, M., Strauss, M., Cartwright, H.N., Ronceray, P., Plitzko, J.M., Förster, F., et al. (2017). The Eukaryotic CO2-Concentrating Organelle Is Liquid-like and Exhibits Dynamic Reorganization. Cell *171*, 148–162.e19. https://doi.org/10.1016/j.cell.2017.08.008.
90. Wietrzynski, W., Schaffer, M., Tegunov, D., Albert, S., Kanazawa, A., Plitzko, J.M., Baumeister, W., and Engel, B.D. (2020). Charting the native

architecture of Chlamydomonas thylakoid membranes with single-molecule precision. eLife *9*, e53740. https://doi.org/10.7554/eLife.53740.

91. Wietrzynski, W., and Engel, B.D. (2023). Supramolecular organization of chloroplast membranes. Chapter 23. In The Chlamydomonas Sourcebook, Third Edition, A.R. Grossman and F.-A. Wollman, eds. (Academic Press), pp. 763–785. https://doi.org/10.1016/B978-0-12-821430-5.00018-3.
92. Peddie, C.J., Genoud, C., Kreshuk, A., Meechan, K., Micheva, K.D., Narayan, K., Pape, C., Parton, R.G., Schieber, N.L., Schwab, Y., et al. (2022). Volume electron microscopy. Nat. Rev. Methods Primers *2*, 51. https://doi.org/10.1038/s43586-022-00131-9.
93. Xu, C.S., Hayworth, K.J., Lu, Z., Grob, P., Hassan, A.M., García-Cerdán, J.G., Niyogi, K.K., Nogales, E., Weinberg, R.J., and Hess, H.F. (2017). Enhanced FIB-SEM systems for large-volume 3D imaging. eLife *6*, e25916. https://doi.org/10.7554/eLife.25916.
94. Purnell, C., Heebner, J., Swulius, M.T., Hylton, R., Kabonick, S., Grillo, M., Grigoryev, S., Heberle, F., Waxham, M.N., and Swulius, M.T. (2023). Rapid Synthesis of Cryo-ET Data for Training Deep Learning Models. Preprint at bioRxiv. https://doi.org/10.1101/2023.04.28.538636.
95. Heebner, J.E., Purnell, C., Hylton, R.K., Marsh, M., Grillo, M.A., and Swulius, M.T. (2022). Deep Learning-Based Segmentation of Cryo-Electron Tomograms. J. Vis. Exp. *189*, e64435. https://doi.org/10.3791/64435.
96. Friedman, J.R., Lackner, L.L., West, M., DiBenedetto, J.R., Nunnari, J., and Voeltz, G.K. (2011). ER tubules mark sites of mitochondrial division. Science *334*, 358–362. https://doi.org/10.1126/science.1207385.
97. Ohad, I., Siekevitz, P., and Palade, G.E. (1967). Biogenesis of chloroplast membranes. I. Plastid dedifferentiation in a dark-grown algal mutant (Chlamydomonas reinhardi). J. Cell Biol. *35*, 521–552. https://doi.org/10.1083/jcb.35.3.521.
98. Hennacy, J.H., Atkinson, N., Kayser-Browne, A., Ergun, S.L., Franklin, E., Wang, L., Eicke, S., Kazachkova, Y., Kafri, M., Fauser, F., et al. (2024). SAGA1 and MITH1 produce matrix-traversing membranes in the CO2-fixing pyrenoid. Nat. Plants *10*, 2038–2051. https://doi.org/10.1038/s41477-024-01847-0.
99. Franklin, E., Wang, L., Renne Cruz, E., Duggal, K., Ergun, S.L., Garde, A., Lunardon, A., Patena, W., Pacini, C., and Jonikas, M.C. (2025). Proteomic analysis of the pyrenoid-traversing membranes of *Chlamydomonas reinhardtii* reveals novel components. Preprint at bioRxiv. https://doi.org/10.1101/2024.10.28.620638.
100. Taylor, T.C., Backlund, A., Bjorhall, K., Spreitzer, R.J., and Andersson, I. (2001). First crystal structure of Rubisco from a green alga, Chlamydomonas reinhardtii. J. Biol. Chem. *276*, 48159–48164. https://doi.org/10.1074/jbc.M107765200.
101. He, S., Chou, H.-T., Matthies, D., Wunder, T., Meyer, M.T., Atkinson, N., Martinez-Sanchez, A., Jeffrey, P.D., Port, S.A., Patena, W., et al. (2020). The structural basis of Rubisco phase separation in the pyrenoid. Nat. Plants *6*, 1480–1490. https://doi.org/10.1038/s41477-020-00811-y.
102. Elad, N., Hou, Z., Dumoux, M., Ramezani, A., Perilla, J.R., and Zhang, P. (2025). In-cell structure and variability of pyrenoid Rubisco. Nat. Commun. *16*, 7763. https://doi.org/10.1101/2025.02.27.640608.
103. Luger, K., Mäder, A.W., Richmond, R.K., Sargent, D.F., and Richmond, T.J. (1997). Crystal structure of the nucleosome core particle at 2.8 A resolution. Nature *389*, 251–260. https://doi.org/10.1038/38444.
104. Fatmaoui, F., Carrivain, P., Taiki, F., Grewe, D., Hagen, W., Jakob, B., Victor, J.-M., Leforestier, A., and Eltsov, M. (2022). Direct visualization and tracing of DNA fold in Drosophila embryo. Preprint at bioRxiv. https://doi.org/10.1101/2022.08.16.502515.
105. Cai, S., Böck, D., Pilhofer, M., and Gan, L. (2018). The in situ structures of mono-, di-, and trinucleosomes in human heterochromatin. Mol. Biol. Cell *29*, 2450–2457. https://doi.org/10.1091/mbc.E18-05-0331.
106. Chen, J.K., Liu, T., Cai, S., Ruan, W., Ng, C.T., Shi, J., Surana, U., and Gan, L. (2025). Nanoscale analysis of human G1 and metaphase chromatin in situ. EMBO J. *44*, 2658–2694. https://doi.org/10.1038/s44318-025-00407-2.
107. Tan, Z.Y., Cai, S., Noble, A.J., Chen, J.K., Shi, J., and Gan, L. (2023). Heterogeneous non-canonical nucleosomes predominate in yeast cells in situ. eLife *12*, RP87672. https://doi.org/10.7554/eLife.87672.
108. Hou, Z., Nightingale, F., Zhu, Y., MacGregor-Chatwin, C., and Zhang, P. (2023). Structure of native chromatin fibres revealed by Cryo-ET in situ. Nat. Commun. *14*, 6324. https://doi.org/10.1038/s41467-023-42072-1.
109. Mittelmeier, T.M., Boyd, J.S., Lamb, M.R., and Dieckmann, C.L. (2011). Asymmetric properties of the Chlamydomonas reinhardtii cytoskeleton direct rhodopsin photoreceptor localization. J. Cell Biol. *193*, 741–753. https://doi.org/10.1083/jcb.201009131.
110. Boyd, J.S., Gray, M.M., Thompson, M.D., Horst, C.J., and Dieckmann, C.L. (2011). The daughter four-membered microtubule rootlet determines anterior-posterior positioning of the eyespot in Chlamydomonas reinhardtii. Cytoskeleton (Hoboken) *68*, 459–469. https://doi.org/10.1002/cm.20524.
111. Tilney, L.G., Bryan, J., Bush, D.J., Fujiwara, K., Mooseker, M.S., Murphy, D.B., and Snyder, D.H. (1973). Microtubules: evidence for 13 protofilaments. J. Cell Biol. *59*, 267–275. https://doi.org/10.1083/jcb.59.2.267.
112. Chalfie, M., and Thomson, J.N. (1982). Structural and functional diversity in the neuronal microtubules of Caenorhabditis elegans. J. Cell Biol. *93*, 15–23. https://doi.org/10.1083/jcb.93.1.15.
113. Foster, H.E., Ventura Santos, C., and Carter, A.P. (2022). A cryo-ET survey of microtubules and intracellular compartments in mammalian axons. J. Cell Biol. *221*, e202103154. https://doi.org/10.1083/jcb.202103154.
114. Chakraborty, S., Martinez-Sanchez, A., Beck, F., Toro-Nahuelpan, M., Hwang, I.-Y., Noh, K.-M., Baumeister, W., and Mahamid, J. (2025). Cryo-ET suggests tubulin chaperones form a subset of microtubule lumenal particles with a role in maintaining neuronal microtubules. Proc. Natl. Acad. Sci. USA *122*, e2404017121. https://doi.org/10.1073/pnas.2404017121.
115. Morris, K.L., Jones, J.R., Halebian, M., Wu, S., Baker, M., Armache, J.-P., Avila Ibarra, A., Sessions, R.B., Cameron, A.D., Cheng, Y., et al. (2019). Cryo-EM of multiple cage architectures reveals a universal mode of clathrin self-assembly. Nat. Struct. Mol. Biol. *26*, 890–898. https://doi.org/10.1038/s41594-019-0292-0.
116. Serwas, D., Akamatsu, M., Moayed, A., Vegesna, K., Vasan, R., Hill, J.M., Schöneberg, J., Davies, K.M., Rangamani, P., and Drubin, D.G. (2022). Mechanistic insights into actin force generation during vesicle formation from cryo-electron tomography. Dev. Cell *57*, 1132–1145.e5. https://doi.org/10.1016/j.devcel.2022.04.012.
117. Dietrich, L., Agip, A.A., Kunz, C., Schwarz, A., and Kühlbrandt, W. (2024). In situ structure and rotary states of mitochondrial ATP synthase in whole Polytomella cells. Science *385*, 1086–1090. https://doi.org/10.1126/science.adp4640.
118. Sheng, X., Watanabe, A., Li, A., Kim, E., Song, C., Murata, K., Song, D., Minagawa, J., and Liu, Z. (2019). Structural insight into light harvesting for photosystem II in green algae. Nat. Plants *5*, 1320–1330. https://doi.org/10.1038/s41477-019-0543-4.
119. Strauss, M., Hofhaus, G., Schröder, R.R., and Kühlbrandt, W. (2008). Dimer ribbons of ATP synthase shape the inner mitochondrial membrane. EMBO J. *27*, 1154–1160. https://doi.org/10.1038/emboj.2008.35.
120. Davies, K.M., Anselmi, C., Wittig, I., Faraldo-Gómez, J.D., and Kühlbrandt, W. (2012). Structure of the yeast F_1F_o-ATP synthase dimer and its role in shaping the mitochondrial cristae. Proc. Natl. Acad. Sci. USA *109*, 13602–13607. https://doi.org/10.1073/pnas.1204593109.
121. Buzzard, E., McLaren, M., Bragoszewski, P., Brancaccio, A., Ford, H.C., Daum, B., Kuwabara, P., Collinson, I., and Gold, V.A.M. (2024). The consequence of ATP synthase dimer angle on mitochondrial morphology studied by cryo-electron tomography. Biochem. J. *481*, 161–175. https://doi.org/10.1042/BCJ20230450.

122. Murphy, B.J., Klusch, N., Langer, J., Mills, D.J., Yildiz, Ö., and Kühlbrandt, W. (2019). Rotary substates of mitochondrial ATP synthase reveal the basis of flexible F1-Fo coupling. Science *364*, eaaw9128. https://doi.org/10.1126/science.aaw9128.

123. Kühlbrandt, W. (2019). Structure and Mechanisms of F-Type ATP Synthases. Annu. Rev. Biochem. *88*, 515–549. https://doi.org/10.1146/annurev-biochem-013118-110903.

124. Vázquez-Acevedo, M., Cardol, P., Cano-Estrada, A., Lapaille, M., Remacle, C., and González-Halphen, D. (2006). The mitochondrial ATP synthase of chlorophycean algae contains eight subunits of unknown origin involved in the formation of an atypical stator-stalk and in the dimerization of the complex. J. Bioenerg. Biomembr. *38*, 271–282. https://doi.org/10.1007/s10863-006-9046-x.

125. Van der Stappen, P., and Waltz, F. (2025). TomoGuide - a cryo-electron tomography processing workflow tutorial. Zenodo. https://doi.org/10.5281/zenodo.15358524.

126. Zhou, K., Gaullier, G., and Luger, K. (2019). Nucleosome structure and dynamics are coming of age. Nat. Struct. Mol. Biol. *26*, 3–13. https://doi.org/10.1038/s41594-018-0166-x.

127. Fierz, B., and Poirier, M.G. (2019). Biophysics of chromatin dynamics. Annu. Rev. Biophys. *48*, 321–345. https://doi.org/10.1146/annurev-biophys-070317-032847.

128. McGinty, R.K., and Tan, S. (2021). Principles of nucleosome recognition by chromatin factors and enzymes. Curr. Opin. Struct. Biol. *71*, 16–26. https://doi.org/10.1016/j.sbi.2021.05.006.

129. Gupte, S.R., Hou, C., Wu, G.-H., Galaz-Montoya, J.G., Chiu, W., and Yeung-Levy, S. (2024). CryoViT: Efficient segmentation of cryogenic electron tomograms with vision foundation models. Preprint at bioRxiv. https://doi.org/10.1101/2024.06.26.600701.

130. Zhao, Y., Bian, H., Mu, M., Uddin, M.R., Li, Z., Li, X., Wang, T., and Xu, M. (2024). Training-free CryoET Tomogram Segmentation. Preprint at arXiv. https://doi.org/10.48550/ARXIV.2407.06833.

131. Huang, Q., Zhou, Y., and Bartesaghi, A. (2024). MiLoPYP: self-supervised molecular pattern mining and particle localization in situ. Nat. Methods *21*, 1863–1872. https://doi.org/10.1038/s41592-024-02403-6.

132. Zeng, X., Kahng, A., Xue, L., Mahamid, J., Chang, Y.-W., and Xu, M. (2023). High-throughput cryo-ET structural pattern mining by unsupervised deep iterative subtomogram clustering. Proc. Natl. Acad. Sci. USA *120*, e2213149120. https://doi.org/10.1073/pnas.2213149120.

133. Liu, G., Niu, T., Qiu, M., Zhu, Y., Sun, F., and Yang, G. (2024). DeepETPicker: Fast and accurate 3D particle picking for cryo-electron tomography using weakly supervised deep learning. Nat. Commun. *15*, 2090. https://doi.org/10.1038/s41467-024-46041-0.

134. Genthe, E., Miletic, S., Tekkali, I., Hennell James, R., Marlovits, T.C., and Heuser, P. (2023). PickYOLO: Fast deep learning particle detector for annotation of cryo electron tomograms. J. Struct. Biol. *215*, 107990. https://doi.org/10.1016/j.jsb.2023.107990.

135. Wagner, T., and Raunser, S. (2020). The evolution of SPHIRE-crYOLO particle picking and its application in automated cryo-EM processing workflows. Commun. Biol. *3*, 61. https://doi.org/10.1038/s42003-020-0790-y.

136. Chen, M., and Ludtke, S.J. (2021). Deep learning-based mixed-dimensional Gaussian mixture model for characterizing variability in cryo-EM. Nat. Methods *18*, 930–936. https://doi.org/10.1038/s41592-021-01220-5.

137. Powell, B.M., and Davis, J.H. (2023). Learning structural heterogeneity from cryo-electron sub-tomograms with tomoDRGN. Nat. Methods *21*, 1525–1536. https://doi.org/10.1101/2023.05.31.542975.

138. Luo, Z., Chen, X., Wang, Q., and Ma, J. (2024). OPUS-TOMO: Towards resolving dynamics and compositional heterogeneities of biomolecules with cryo-electron tomography. Preprint at bioRxiv. https://doi.org/10.1101/2024.06.30.601442.

139. Li, X., Yan, X., Li, S., Huang, W., Wang, H., Zhao, T., Huang, M., Zhou, N., and Shen, Y. (2024). MPicker: Visualizing and picking membrane proteins for cryo-electron tomography. Nat. Commun. *16*, 472. https://doi.org/10.1038/s41467-024-55767-w.

140. Kreysing, J.P., Cruz-Leon, S., Betz, J., Penzo, C., Majtner, T., Schreiber, M., Turonova, B., Lusic, M., Hummer, G., and Beck, M. (2025). Molecular architecture of heterochromatin at the nuclear periphery of primary human cells. Preprint at bioRxiv. https://doi.org/10.1101/2025.04.09.647790.

141. He, S., Wu, Z., Tian, Y., Yu, Z., Yu, J., Wang, X., Li, J., Liu, B., and Xu, Y. (2020). Structure of nucleosome-bound human BAF complex. Science *367*, 875–881. https://doi.org/10.1126/science.aaz9761.

142. Michael, A.K., Grand, R.S., Isbel, L., Cavadini, S., Kozicka, Z., Kempf, G., Bunker, R.D., Schenk, A.D., Graff-Meyer, A., Pathare, G.R., et al. (2020). Mechanisms of OCT4-SOX2 motif readout on nucleosomes. Science *368*, 1460–1465. https://doi.org/10.1126/science.abb0074.

143. Dodonova, S.O., Zhu, F., Dienemann, C., Taipale, J., and Cramer, P. (2020). Nucleosome-bound SOX2 and SOX11 structures elucidate pioneer factor function. Nature *580*, 669–672. https://doi.org/10.1038/s41586-020-2195-y.

144. Farnung, L., Vos, S.M., and Cramer, P. (2018). Structure of transcribing RNA polymerase II-nucleosome complex. Nat. Commun. *9*, 5432. https://doi.org/10.1038/s41467-018-07870-y.

145. Kujirai, T., Ehara, H., Fujino, Y., Shirouzu, M., Sekine, S.-I., and Kurumizaka, H. (2018). Structural basis of the nucleosome transition during RNA polymerase II passage. Science *362*, 595–598. https://doi.org/10.1126/science.aau9904.

146. He, Y., Yan, C., Fang, J., Inouye, C., Tjian, R., Ivanov, I., and Nogales, E. (2016). Near-atomic resolution visualization of human transcription promoter opening. Nature *533*, 359–365. https://doi.org/10.1038/nature17970.

147. Plaschka, C., Lin, P.-C., Charenton, C., and Nagai, K. (2018). Prespliceosome structure provides insights into spliceosome assembly and regulation. Nature *559*, 419–422. https://doi.org/10.1038/s41586-018-0323-8.

148. Pacheco-Fiallos, B., Vorländer, M.K., Riabov-Bassat, D., Fin, L., O'Reilly, F.J., Ayala, F.I., Schellhaas, U., Rappsilber, J., and Plaschka, C. (2023). mRNA recognition and packaging by the human transcription-export complex. Nature *616*, 828–835. https://doi.org/10.1038/s41586-023-05904-0.

149. Jin, Z., Wan, L., Zhang, Y., Li, X., Cao, Y., Liu, H., Fan, S., Cao, D., Wang, Z., Li, X., et al. (2022). Structure of a TOC-TIC supercomplex spanning two chloroplast envelope membranes. Cell *185*, 4788–4800.e13. https://doi.org/10.1016/j.cell.2022.10.030.

150. Liu, H., Li, A., Rochaix, J.-D., and Liu, Z. (2023). Architecture of chloroplast TOC-TIC translocon supercomplex. Nature *615*, 349–357. https://doi.org/10.1038/s41586-023-05744-y.

151. Brown, C.M., Westendorp, M.S.S., Zarmiento-Garcia, R., Stevens, J.A., Bruininks, B.M.H., Rouse, S.L., Marrink, S.J., and Wassenaar, T.A. (2025). An integrative modelling approach to the mitochondrial cristae. Commun. Biol. *8*, 972. https://doi.org/10.1038/s42003-025-08381-5.

152. Stevens, J.A., Grünewald, F., van Tilburg, P.A.M., König, M., Gilbert, B.R., Brier, T.A., Thornburg, Z.R., Luthey-Schulten, Z., and Marrink, S.J. (2023). Molecular dynamics simulation of an entire cell. Front. Chem. *11*, 1106495. https://doi.org/10.3389/fchem.2023.1106495.

153. Diogo Righetto, R. (2024). EMPIAR-11830 dataset annotation: in situ cryo-electron tomography of Chlamydomonas reinhardtii. Zenodo. https://doi.org/10.5281/zenodo.13941456.

154. Umen, J.G., and Goodenough, U.W. (2001). Control of cell division by a retinoblastoma protein homolog in Chlamydomonas. Genes Dev. *15*, 1652–1661. https://doi.org/10.1101/gad.892101.

155. Ermel, U.H., Arghittu, S.M., and Frangakis, A.S. (2022). ArtiaX: An electron tomography toolbox for the interactive handling of sub-tomograms

in UCSF ChimeraX. Protein Sci. *31*, e4472. https://doi.org/10.1002/pro.4472.

156. Grant, T., Rohou, A., and Grigorieff, N. (2018). cisTEM, user-friendly software for single-particle image processing. eLife *7*, e35383. https://doi.org/10.7554/eLife.35383.
157. Rohou, A., and Grigorieff, N. (2015). CTFFIND4: Fast and accurate defocus estimation from electron micrographs. J. Struct. Biol. *192*, 216–221. https://doi.org/10.1016/j.jsb.2015.08.008.
158. Kremer, J.R., Mastronarde, D.N., and McIntosh, J.R. (1996). Computer visualization of three-dimensional image data using IMOD. J. Struct. Biol. *116*, 71–76. https://doi.org/10.1006/jsbi.1996.0013.
159. Zheng, S.Q., Palovcak, E., Armache, J.-P., Verba, K.A., Cheng, Y., and Agard, D.A. (2017). MotionCor2: anisotropic correction of beam-induced motion for improved cryo-electron microscopy. Nat. Methods *14*, 331–332. https://doi.org/10.1038/nmeth.4193.
160. Zivanov, J., Nakane, T., Forsberg, B.O., Kimanius, D., Hagen, W.J., Lindahl, E., and Scheres, S.H. (2018). New tools for automated high-resolution cryo-EM structure determination in RELION-3. eLife *7*, e42166. https://doi.org/10.7554/eLife.42166.
161. Kimanius, D., Dong, L., Sharov, G., Nakane, T., and Scheres, S.H.W. (2021). New tools for automated cryo-EM single-particle analysis in RELION-4.0. Biochem. J. *478*, 4169–4185. https://doi.org/10.1042/BCJ20210708.
162. Righetto, R., and Lamm, L. (2024). CellArchLab/slabify-et: v0.3.0. Zenodo. https://doi.org/10.5281/zenodo.13941081.
163. Khavnekar, S., and Wan, W. (2025). An approach for coherent periodogram averaging of tilt-series data for improved contrast transfer function estimation. FEBS Open Bio *15*, 1209–1218. https://doi.org/10.1002/2211-5463.70050.
164. Khavnekar, S., Erdmann, P.S., and Wan, W. (2024). TOMOMAN: a software package for large scale cryo-electron tomography data preprocessing, community data sharing, and collaborative computing. Preprint at bioRxiv. https://doi.org/10.1101/2024.05.02.589639.
165. Pettersen, E.F., Goddard, T.D., Huang, C.C., Couch, G.S., Greenblatt, D.M., Meng, E.C., and Ferrin, T.E. (2004). UCSF Chimera–a visualization system for exploratory research and analysis. J. Comput. Chem. *25*, 1605–1612. https://doi.org/10.1002/jcc.20084.
166. Goddard, T.D., Huang, C.C., Meng, E.C., Pettersen, E.F., Couch, G.S., Morris, J.H., and Ferrin, T.E. (2018). UCSF ChimeraX: Meeting modern challenges in visualization and analysis. Protein Sci. *27*, 14–25. https://doi.org/10.1002/pro.3235.
167. Tegunov, D., and Cramer, P. (2019). Real-time cryo-electron microscopy data preprocessing with Warp. Nat. Methods *16*, 1146–1152. https://doi.org/10.1038/s41592-019-0580-y.
168. Tegunov D., Burt A., Shah P.N.M., and Wachsmuth-Melm, M. (2024). warpem/warp: v2.0.0dev31. Zenodo. https://doi.org/10.5281/ZENODO.13982246.
169. Khavnekar, S., Erdmann, P.S., and Wan, W. (2024). TOMOMAN: a software package for large-scale cryo-electron tomography data preprocessing, community data sharing and collaborative computing. J. Appl. Crystallogr. *57*, 2010–2016. https://doi.org/10.1107/S1600576724010264.
170. Zheng, S., Wolff, G., Greenan, G., Chen, Z., Faas, F.G.A., Bárcena, M., Koster, A.J., Cheng, Y., and Agard, D.A. (2022). AreTomo: An integrated software package for automated marker-free, motion-corrected cryo-electron tomographic alignment and reconstruction. J. Struct. Biol. X *6*, 100068. https://doi.org/10.1016/j.yjsbx.2022.100068.
171. Zivanov, J., Otón, J., Ke, Z., von Kügelgen, A., Pyle, E., Qu, K., Morado, D., Castaño-Díez, D., Zanetti, G., Bharat, T.A.M., et al. (2022). A Bayesian approach to single-particle electron cryo-tomography in RELION-4.0. eLife *11*, e83724. https://doi.org/10.7554/eLife.83724.
172. Mastronarde, D.N., and Held, S.R. (2017). Automated tilt series alignment and tomographic reconstruction in IMOD. J. Struct. Biol. *197*, 102–113. https://doi.org/10.1016/j.jsb.2016.07.011.
173. Righetto, R., and LorenzLamm. (2024). CellArchLab/slabify-et: v0.2.0 (v0.2.0). Zenodo. https://doi.org/10.5281/zenodo.13941082v.
174. Pellegrino, S., Demeshkina, N., Mancera-Martinez, E., Melnikov, S., Simonetti, A., Myasnikov, A., Yusupov, M., Yusupova, G., and Hashem, Y. (2018). Structural insights into the role of diphthamide on elongation factor 2 in mRNA reading-frame maintenance. J. Mol. Biol. *430*, 2677–2687. https://doi.org/10.1016/j.jmb.2018.06.006.
175. Himes, B., and Grigorieff, N. (2021). Cryo-TEM simulations of amorphous radiation-sensitive samples using multislice wave propagation. IUCrJ *8*, 943–953. https://doi.org/10.1107/s2052252521008538.
176. Milicevic, N., Jenner, L., Myasnikov, A., Yusupov, M., and Yusupova, G. (2024). mRNA reading frame maintenance during eukaryotic ribosome translocation. Nature *625*, 393–400. https://doi.org/10.1038/s41586-023-06780-4.
177. Tachiwana, H., Kagawa, W., Osakabe, A., Kawaguchi, K., Shiga, T., Hayashi-Takanaka, Y., Kimura, H., and Kurumizaka, H. (2010). Structural basis of instability of the nucleosome containing a testis-specific histone variant, human H3T. Proc. Natl. Acad. Sci. USA *107*, 10454–10459. https://doi.org/10.1073/pnas.1003064107.
178. Meng, E.C., Goddard, T.D., Pettersen, E.F., Couch, G.S., Pearson, Z.J., Morris, J.H., and Ferrin, T.E. (2023). UCSF ChimeraX: Tools for structure building and analysis. Protein Sci. *32*, e4792. https://doi.org/10.1002/pro.4792.
179. Chaillet, M.L., Roet, S., Veltkamp, R.C., and Förster, F. (2025). pytom-match-pick: A tophat-transform constraint for automated classification in template matching. J. Struct. Biol. X *11*, 100125. https://doi.org/10.1016/j.yjsbx.2025.100125.
180. Rosenthal, P.B., and Henderson, R. (2003). Optimal determination of particle orientation, absolute hand, and contrast loss in single-particle electron cryomicroscopy. J. Mol. Biol. *333*, 721–745. https://doi.org/10.1016/j.jmb.2003.07.013.
181. Rigort, A., Günther, D., Hegerl, R., Baum, D., Weber, B., Prohaska, S., Medalia, O., Baumeister, W., and Hege, H.-C. (2012). Automated segmentation of electron tomograms for a quantitative description of actin filament networks. J. Struct. Biol. *177*, 135–144. https://doi.org/10.1016/j.jsb.2011.08.012.
182. Chakraborty, S., Mahamid, J., and Baumeister, W. (2020). Cryoelectron Tomography Reveals Nanoscale Organization of the Cytoskeleton and Its Relation to Microtubule Curvature Inside Cells. Structure *28*, 991–1003.e4. https://doi.org/10.1016/j.str.2020.05.013.
183. Qu, K., Glass, B., Doležal, M., Schur, F.K.M., Murciano, B., Rein, A., Rumlová, M., Ruml, T., Kräusslich, H.-G., and Briggs, J.A.G. (2018). Structure and architecture of immature and mature murine leukemia virus capsids. Proc. Natl. Acad. Sci. USA *115*, E11751–E11760. https://doi.org/10.1073/pnas.1811580115.
184. Sosa, H., and Chrétien, D. (1998). Relationship between moiré patterns, tubulin shape, and microtubule polarity. Cell Motil. Cytoskeleton *40*, 38–43. https://doi.org/10.1002/(SICI)1097-0169(1998)40:1<38::AID-CM4>3.0.CO;2-B.
185. Pettersen, E.F., Goddard, T.D., Huang, C.C., Meng, E.C., Couch, G.S., Croll, T.I., Morris, J.H., and Ferrin, T.E. (2021). UCSF ChimeraX: Structure visualization for researchers, educators, and developers. Protein Sci. *30*, 70–82. https://doi.org/10.1002/pro.3943.
186. Scheres, S.H.W., and Chen, S. (2012). Prevention of overfitting in cryo-EM structure determination. Nat. Methods *9*, 853–854. https://doi.org/10.1038/nmeth.2115.
187. Hall, S.R. (1991). The STAR file: a new format for electronic data transfer and archiving. J. Chem. Inf. Comput. Sci. *31*, 326–333. https://doi.org/10.1021/ci00002a020.

STAR★METHODS

KEY RESOURCES TABLE

REAGENT or RESOURCE	SOURCE	IDENTIFIER
Experimental models: Organisms/strains		
Chlamydomonas reinhardtii strain mat3-4	Umen and Goodenough[154] Chlamydomonas Resource Center, University of Minnesota	CC3994
Deposited data		
Raw and pre-processed cryo-ET data	This paper	EMPIAR-11830
Raw Auto Slice and View data	This paper	EMPIAR-11275
Cellular tomograms	This paper	EMPIAR-11830 and DS-10302
80S ribosome subtomogram average	This paper	EMD-51847
Rubisco subtomogram average	This paper	EMD-51848
Nucleosome subtomogram average	This paper	EMD-19906
Photosystem II subtomogram average	This paper	EMD-51731
Microtoubules subtomogram average	This paper	EMD-51804
Clathrin subtomogram average	This paper	EMD-51789
ATP synthase peripheral stalk subtomogram average	This paper	EMD-51802
Particle coordinates	This paper	https://github.com/Chromatin-Structure-Rhythms-Lab/ChlamyAnnotations
Manually annotated tomogram list	This paper	https://doi.org/10.5281/zenodo.13941455
Nucleoplasm masks	This paper	https://doi.org/10.5281/zenodo.16619468
Tomogram segmentations (Figures 2 and 3)	This paper	https://doi.org/10.5281/zenodo.15875785
Correspondence between tomogram names and TOMOMAN numbers	This paper	https://ftp.ebi.ac.uk/empiar/world_availability/11830/data/chlamy_visual_proteomics/tomolist_num_dir.star
Software and algorithms		
Amira v2021.2	Thermo Fisher Scientific	https://www.thermofisher.com/us/en/home/industrial/electron-microscopy/electron-microscopy-instruments-workflow-solutions/3d-visualization-analysis-software/amira-life-sciences-biomedical.html
ArtiaX	Ermel et al.[155]	https://github.com/FrangakisLab/ArtiaX
Auto Slice & View 5	Thermo Fisher Scientific	https://www.thermofisher.com/ch/en/home/electron-microscopy/products/software-em-3d-vis/auto-slice-view-4-software.html
cisTEM	Grant et al.[156]	https://doi.org/10.7554/eLife.35383
cryo-CARE v0.2.1	Buchholz et al.[67]	https://github.com/juglab/cryoCARE_pip
CryoTomoSim v0.6.0	Purnell et al.[94]	https://github.com/carsonpurnell/cryotomosim_CTS
CTFFIND v4.1.14	Rohou and Grigorieff[157]	https://grigorieff lab.umassmed.edu/ctffind4
DragonFly v2022.1	Object Research Systems	https://dragonfly.comet.tech/
IMOD v4.11	Kremer et al.[158]	https://bio3d.colorado.edu/imod/index.html
M v1.0.9	Tegunov et al.[31]	https://warpem.github.io/

(*Continued on next page*)

Continued

REAGENT or RESOURCE	SOURCE	IDENTIFIER
MATLAB R2022b	MathWorks	https://www.mathworks.com/products/matlab.html
MemBrain v2	Lamm et al.[49]	https://github.com/CellArchLab/MemBrain-v2
MotionCorr v2.1	Zheng et al.[159]	https://emcore.ucsf.edu/ucsf-software
pytom-match-pick	Chaillet et al.[30]	https://github.com/SBC-Utrecht/pytom-match-pick
RELION v3.1	Zivanov et al.[160]	https://relion.readthedocs.io/en/release-3.1/
RELION v4.0	Kimanius et al.[161]	https://relion.readthedocs.io/en/release-4.0/
Slabify	Righetto and Lamm[162]	https://github.com/CellArchLab/slabify-et
STOPGAP	Wan et al.[28]	https://github.com/wan-lab-vanderbilt/STOPGAP
Tomography 5.11 software	Thermo Fisher Scientific	https://www.thermofisher.com/ch/en/home/electron-microscopy/products/software-em-3d-vis/tomography-software.html
TILTCTF	Khavnekar and Wan[163]	https://github.com/wan-lab-vanderbilt/TOMOMAN
TOMOMAN v0.9	Khavnekar et al.[164]	https://github.com/wan-lab-vanderbilt/TOMOMAN
UCSF Chimera	Pettersen et al.[165]	https://www.rbvi.ucsf.edu/chimera/
UCSF ChimeraX	Goddard et al.[166]	https://www.rbvi.ucsf.edu/chimerax/
Warp v1.0.9	Tegunov and Cramer[167]	https://warpem.github.io/
WarpTools v2.0.0	Tegunov et al.[167,168]	https://github.com/warpem/warp
Other		
R 2/1 holey carbon-foil 200-mesh copper EM grids	Quantifoil Micro Tools	Cat#N1-c15ncu20-01
R 1/4 SiO2-foil 200-mesh gold EM grids	Quantifoil Micro Tools	Cat#N1-S13nAu20-01
Arctis cryo-PFIB-SEM	Thermo Fisher Scientific	https://www.thermofisher.com/ch/en/home/electron-microscopy/products/dualbeam-fib-sem-microscopes/arctis-cryo-pfib.html
Hydra Bio cryo-PFIB-SEM	Thermo Fisher Scientific	https://www.thermofisher.com/ch/en/home/electron-microscopy/products/dualbeam-fib-sem-microscopes/hydra-bio-plasma-fib.html
Titan Krios 300 kV TEM	Thermo Fisher Scientific	https://www.thermofisher.com/ch/en/home/electron-microscopy/products/transmission-electron-microscopes/krios-cryo-tem.html
Vitrobot Mark IV plunger	Thermo Fisher Scientific	https://www.thermofisher.com/ch/en/home/electron-microscopy/products/sample-preparation-equipment-em/vitrobot/instruments/vitrobot-mark-iv.html
chlamydataset2relion5: script to import pre-processed data into RELION-5	Righetto and Van der Stappen	https://github.com/Chromatin-Structure-Rhythms-Lab/ChlamyAnnotations
TomoGuide: subtomogram averaging teaching resource	Van der Stappen and Waltz[125]	https://tomoguide.github.io/

EXPERIMENTAL MODEL AND STUDY PARTICIPANT DETAILS

Algae strain and culture

Cells used in this study were *Chlamydomonas reinhardtii* strain mat3-4 (CC3994), obtained from the Chlamydomonas Resource Center, University of Minnesota, MN (funded by the US National Science Foundation). This strain has a smaller cell phenotype,[154] which is advantageous for vitrification. From an agar plate stock culture, a liquid culture was inoculated in 40 mL Tris-acetate phosphate (TAP) media, containing 0.02 M Tris base, TAP salts (7.00 mM NH_4Cl, 0.83 mM, $MgSO_4$, 0.45 mM $CaCl_2$), Phosphate buffer (1.65 mM K_2HPO_4, 1.05 mM KH_2PO_4), and Hunter trace elements (0.134 mM Na_2EDTA, 0.136 mM $ZnSO_4$, 0.184 mM H_3BO_4, 40 µM $MnCl_2$, 32.9 µM $FeSO_4$, 12.3 µM $CoCl_2$, 10.0 µM $CuSO_4$, 4.44 µM $(NH_4)_6MoO_3$, 17.5 mM acetic acid). Cells were constantly illuminated (~90 µmol photons/m^2s), agitated at 100 rpm in normal atmosphere, and harvested 48–72 h after inoculation.

METHOD DETAILS

Cell vitrification

A total of 4 µL of cell suspension (1500–2000 cells/µL) were applied to holey carbon R2/1 or R1/4 copper TEM grids (Quantifoil), and cells were plunge frozen on a Vitrobot Mark IV (Thermo Fisher Scientific, settings: blot force = 10, blot time = 10 s, temperature = 30 °C, humidity = 90%) using back-side blotting and either an ethane/propane or an ethane bath. Samples were stored in liquid nitrogen until use.

Serial cryo-FIB/SEM volume imaging

Sample grids were clipped in Autogrids (Thermo Fisher Scientific) and subjected to automated serial slice FIB/SEM volume imaging using Auto Slice & View 5 (Thermo Fisher Scientific) in a Hydra Bio PFIB dual beam instrument (Thermo Fisher Scientific). Grids were loaded using the standard 35° pre-tilted holder, then coated with conductive and protective layers including: Pt sputter (magnetron, 30 mA, 10 pA, 30 sec); organometallic Pt condensate using gas injection system (2 min); Pt sputter (magnetron, 30 mA, 10 pA, 30 sec). For serial FIB/SEM volume imaging, these samples were tilted such that the grid is flat and perpendicular to the electron beam (i.e., 35° stage tilt), resulting in a FIB milling angle of 38°. Sites were milled using argon with 30 kV accelerating voltage and 200 pA nominal beam current. Slice thickness was 20 nm. SEM imaging conditions were optimized with 1.2 kV accelerating voltage and 13 pA beam current using immersion mode with TLD-DH detector settings. Image collection parameters were 50 ns dwell time with 150 line integrations and a 5 x 5 nm pixel size.

Cryo-FIB lamella preparation

Grids were clipped into Autogrids (Thermo Fisher Scientific) and subjected to automated lamella preparation using an Arctis cryo-plasma-FIB (Thermo Fisher Scientific) with two different workflows. For the first workflow, prior to milling, grids were coated with a layer of ion-sputtered, metallic platinum (Pt) for 120 sec (Xe+, 12 kV, 70 nA). This was followed by 400 nm organometallic Pt using the gas injection system, then an additional ion-sputtered platinum layer (Xe+, 12 kV, 70 nA, 120 sec). Next, grids were surveyed using Maps software (Thermo Fisher Scientific) for lamella site identification followed by automated lamella preparation using AutoTEM Cryo with a thickness range set between 150–300 nm for polishing steps. The second workflow was performed with Arctis WebUI (Thermo Fisher Scientific). Using the WebUI interface, grids were screened automatically, coated with the same amount of Pt sputtering-GIS-sputtering as in the first workflow, then subjected to automated lamella preparation. All FIB milling was performed using xenon or argon ions (Tables S1 and S2).

Cryo-ET data acquisition

Datasets were collected using a Krios G4 equipped with a Selectris X energy filter and Falcon 4i direct electron detector (Thermo Fisher Scientific). Tilt-series were collected with a dose-symmetric tilt scheme using TEM Tomography 5 software (Thermo Fisher Scientific). The tilt span of ± 60° was used with 2° or 3° steps starting at either ± 10° to compensate for the lamella milling angle. Target focus was set for each tilt-series in steps of 0.25 µm over a range of -1.5 µm to -3.5 µm. Data was acquired in EER mode of Falcon 4i with a nominal pixel size of 1.96 Å and a total dose of 3.5 e^-/Å2 per tilt. A 10 eV slit was used for the entire data collection. Eucentric height estimation was performed once for each lamella using stage tilt method in TEM Tomography 5 software. Regions of interest were added manually, and positions saved. Tracking and focusing was performed before and after acquisition of each tilt step. The energy filter zero-loss peak was tuned once before each data acquisition session.

Preprocessing

The data were preprocessed using TOMOgram MANager (TOMOMAN).[169] EER images were motion corrected using a modified version (to generate odd-even frame sums) of RELION's implementation of MotionCor2.[159] The defocus was estimated using tilt-corrected periodogram averaging in tiltCTF[163] along with CTFFIND4[157] implementation within TOMOMAN. Tilt-series were aligned using fiducial-less alignment in AreTomo.[170] Initially, tomograms without CTF correction were reconstructed by IMOD's tilt program. Subsequent odd-even reconstructions and denoised tomograms were generated using cryo-CARE. 3D-CTF corrected reconstructions were generated with novaCTF using phase-flipping algorithm in batch. All tomographic reconstructions were downsampled (binned) using the Fourier3D program (https://github.com/turonova/Fourier3D) when applicable. Exporting to Warp-RELION-M[31,167] and RELION-4[171] tomography workflows was performed using TOMOMAN for STA. All operations were performed in batch mode as implemented in TOMOMAN.

Dataset cleaning and curation

Manual curation of the dataset was performed at two stages: 1) after acquisition, tilt-series were inspected to discard whole tilt-series or individual tilts that were obstructed or blurry; 2) after reconstruction, poorly aligned tomograms were excluded to yield the final set of 1829.

Lamella thickness measurement

Lamella thickness was measured in each reconstructed tomogram (Figure 1E) through a TOMOMAN script based on IMOD's findsection program.[172] In cases where findsection failed to estimate a boundary model due to low tomogram contrast, an indirect measurement was made based on boundary masks automatically generated with Slabify.[173]

Regression denoising

Synthetic cryo-ET data for regression U-net training was generated using CryoTomoSim.[94] Using a box of 400 x 400 x 50 pixels, a mixture of medium and small proteins were modelled in four layers at 7.84 Å/px. The exact protein identities are not important to training. Ten membrane vesicles were modelled. Particle density was 0.8, the vitreous ice option was used, and the iterations for each layer were 500, 500, 4000, 8000. The output ("ideal" tomogram) was simulated at -1 μm defocus, -89 to 89 tilt, 0.5 degree tilt increment and total dose = 0. The input (noisy tomogram) was simulated at -3 μm defocus, -60 to 60 tilt, 3 degree tilt increment, and total dose = 80. Both datasets were loaded into Dragonfly 2022.2 (Object Research Systems) and used as training input and output for a regression 2.5D U-net with the following architecture: depth level 5, initial filter count 64, slice count 5, patch size 128, Loss function ORSMixedGradientLoss. Training proceeded for 46 epochs using a total of 15,840 patches. The trained regression U-Net was used to denoise thylakoid tomograms prior to segmentation with a segmentation U-Net (described below).

Segmentation of cryo-ET data

A combination of shallow and 2D U-nets were trained using Amira 2023.2 (Thermo Fisher Scientific) to segment ribosomes, COPI, nuclear pore complexes, microtubules (singlets and triplets), basal body cartwheel, and Rubisco in Figure 2. Approximately 200 patches from each tomogram were selected after hand annotation for AI-assisted segmentation. The resulting segmentation was used for further patch extraction to train a U-net of the following architecture: 2D, backbone: resnet18, patch size: 128, loss function: dice. The 2.5D segmentation U-net for PSII was trained using Dragonfly 2022.2 (Object Research Systems) according to a previously described protocol.[95] In brief, Segmentation Wizard was used for manual annotation of 5-6 training slices, and a generic U-net of the following architecture was trained: 2.5D: 3 slices, depth level: 5, initial filter count: 64, patch size: 128. Training data included slices from tomograms numbered 24, 373, 473, and 900. Aside from patch size, all hyperparameters were left as default. Training labels were membrane, ATP synthase, ribosomes, PSII and background. The 2.5D segmentation U-nets for Figure 3 segmentations were trained using Dragonfly 2022.2 (Object Research Systems) according to the same protocol using the following architecture: Pretrained U-net, 3-slices, depth level: 5, initial filter count: 64, patch size: 96. Unique U-nets were trained for each segmentation. All membrane segmentations (Figures 2C–2H and 3) were obtained using the MemBrain-seg module of the MemBrain v2 package.[49] ATP synthase (yellow label in Figures 2F, 3A, and 3B), nucleosomes (pink label in Figure 2C), and ribosomes (orange label in Figures 2C–2G, 3A, and 3B) are particle mapbacks of the STA maps at template matching coordinates.

Segmentation of FIB-SEM volume EM data

A combination of image processing workflows and deep learning segmentation were used to segment the whole Chlamydomonas cell in Figure 2A. Most organelles were segmented using manual annotation combined with the interpolation tool in Amira's Segmentation+ workroom. The chloroplast was segmented by creating a ground truth training set with manual annotation then training an AI-assisted segmentation model (VGG16 UNet) that was applied to the full volume. The manually and deep learning created labels were combined for final visualization.

STA: 80S Ribosome

Initial ribosome positions and orientations were determined by template matching using STOPGAP[28] or its GPU implementation GAPSTOP-TM[26] (https://gitlab.mpcdf.mpg.de/bturo/gapstop_tm) on ∼1000 8x binned tomograms, resulting in ∼500,000 particles. The template density for the 80S ribosome was simulated using PDB: 6GQV[174] and the simulate program[175] of the cisTEM package.[156] These particles were extracted at 4x binning and iteratively aligned using STOPGAP and a soft mask shaped to contours of the full ribosome density. The initial reference for alignment was generated using the ∼500,000 particles picked with template matching. Gradually reducing the local angular cone search was performed with two iterations each of 5 degrees with 3 steps followed by 3 degrees with 3 steps at 4x binning. After these initial subtomogram averaging iterations, particle cross-correlation scores were distributed bimodally, indicating a separation between true and false particles. The ∼140,000 particles in the higher-scoring distribution were selected for further processing. These particles were further aligned at 2x binning, first using a full ribosome mask (three iterations of 2 degrees with 3 steps), followed by alignment using a mask focused on the large subunit (one iteration of 1 degree with 3 steps). The resulting orientations were used as a starting point for two separate multireference alignment (MRA) runs in STOPGAP (Figures S2E–S2G). Starting references were generated by randomly assigning 20% of the dataset to ten classes. To classify the membrane bound state, MRA was performed with a mask focusing on the membrane bound region. To classify the different tRNA states, MRA was performed with a mask focusing on the tRNA channel. In both cases, the first 10 iterations of MRA were performed using simulated annealing, followed by MRA with stochastic hill climbing and without simulated annealing until convergence, i.e., when less than 1% of subtomograms changed classes between iterations. Final classes were assigned by visually inspecting the class averages and merging identical states. This resulted in five unique states: 'A, P unrotated', 'A, P rotated', 'eEF2, A/P, P/E rotated', 'eEF2, P, E partial rotated', and 'eEF1A, A/T, P unrotated'[176] (Figure S2G). For higher resolution averaging, particles were exported to Warptools[168] at 1x binning (1.96 Å/px) using TOMOMAN.[169] After importing, three iterations of M were performed with 2D image warp refinement, particle pose refinement, and exhaustive CTF refinement. Of these, the last iteration was refined for tilt angles. This resulted in the 80S ribosome density map at global resolution of 4.0 Å from ∼140,000 particles from 600 tomograms (Figures 1F and S2D). For analyzing the relationship between Rosenthal-Henderson B-factor and lamella thickness (Figures 1G and S3A), particles were segregated based on the thickness of the corresponding tomogram. Thickness bins were defined as 100-125, 125-150, 150-175, 175-200, 200-225, 225-250, >250 nm. To analyze the damage due to FIB milling (Figures 1H and S3B), we calculated Rosenthal-Henderson B-factor for particles based on the distance of the particle center (depth) from the edge of the lamella (tomogram boundary model). Depth bins were defined as 0-15, 15-30, 30-45, 45-60, 60-75, 75-90, 90-105, >105 nm from the lamella surface. In both these cases, we used the boundary models created during the tomogram thickness measurements (see "lamella thickness measurement" section above). For each thickness and depth bin, Rosenthal-Henderson B-factor was calculated based on the linear fit of resolution^{-2} vs. ln(number of particles) for subsets with 2000, 4000, 6000, 8000, and 10000 particles (Figure S3).

STA: Rubisco

The template map was generated from PDB: 1GK8[100] using the "simulate" program within the cisTEM package.[156] This map was used to determine initial Rubisco positions and orientations by template matching in STOPGAP on 16 4x binned tomograms (Figures S4A and S4B), resulting in approximately ∼240,000 particles. These subvolumes were then iteratively aligned using STOPGAP at 4x and 2x binning using a soft mask shaped to contours of the full Rubisco holocomplex density. The resulting orientations were used as a starting point for an MRA protocol in STOPGAP. The initial reference for alignment was generated from the ∼240,000 particles picked with template matching. Local angular cone search was performed with two iterations of 6 degrees with 3 steps at 4x binning. This was followed by gradually reducing the local angular cone search at 2x binning with two iterations of 5 degrees with 3 steps followed by one iteration of 3 degrees with 3 steps. After classification, particles were exported to Warp[167] and RELION v3.0[160] at 1x binning (1.96 Å/px) using TOMOMAN.[169] After additional 3D classification using RELION v3.0 (Figure S4C), we obtained a 7.5 Å class average from ∼14,000 particles (Figures 4C, S4D, and S4E). The final average was obtained with D4 symmetry applied during the 3D refinement.

STA: Nucleosomes

126 tomograms from the curated dataset containing nuclei in the field of view were selected for processing based on their visual quality. For particle picking, first with a subset of 8 tomograms, we applied STOPGAP[28] for template matching on 4x binned tomograms. The template map was generated from PDB: 3AFA[177] at 7.84 Å/px using the molmap command in ChimeraX.[178] Subtomograms were reconstructed at 3.92 Å/px (2x binning) in Warp and then subjected to iterative rounds of alignment and classification, followed by 3D auto-refinement in RELION v3.1.4.[160] The resulting nucleosome map (∼15 Å) was then used as a template to pick particles within the entire set of 126 tomograms using the GPU-accelerated version of PyTom[30,179] for template matching (https://github.com/SBC-Utrecht/pytom-match-pick) on 4x binned tomograms (Figures S5A and S5B). In order to exclude obviously false cross-correlation peaks outside the nucleus, nuclear masks were predicted by a neural network using MemBrain-seg,[49] which was trained with 8x binned segmentations manually created with Amira (Thermo Fisher Scientific). Up to 8,000 putative particles were extracted from each tomogram following standard PyTom template matching procedures, yielding a total of 223,507 particles. Subtomograms were reconstructed at 3.92 Å/px (2x binning) in Warp and then subjected to multiple rounds of 3D classification and 3D auto-refinement in RELION v3.1.4.[160] The best class, containing 23,878 particles (Figures S5C and S5D), was then exported back to Warp[167] for subtomogram extraction using custom TOMOMAN scripts.[169] Subsequently, multi-particle refinement was performed in M[31] to refine particle poses as well as parameters of the tilt-series geometry and the contrast transfer function (CTF). Refinements in M and RELION were iterated at 2x and 1x binning (1.96 Å/px) until convergence, yielding a nucleosome map at a global resolution of 9.6 Å according to the Fourier shell correlation 0.143 threshold[180] (Figures 4A and S5E–S5I). The final refinement in M was performed with an input mask around the histone octamer core, excluding the DNA.

STA: Microtubules

The STA procedure for the MTs was performed essentially as described before.[114] MTs in 8x binned tomograms (15.68 Å/px) were segmented with the automated template-matching procedure in Amira software v.6.2.0 (Thermo Fisher Scientific) as previously described[181,182] using a generic template of a missing wedge-modulated 120 nm long hollow cylinder with outer and inner radii of 14 and 7 nm, respectively (Figures S6A and S6B). The coordinates of the traced MT center lines were further resampled in MATLAB (MathWorks) to obtain equidistant points at every 3.2 nm. Resampled coordinates were used to generate a tubular grid around the center line and place points approximately on each tubulin subunit taking into account inter-subunit distance of 40 Å along the filament z-axis and 60 Å around the helix. These positions were oversampled 2x, and ~315,000 subtomograms were extracted from these grid points. Each MT in a given tomogram was assigned a class number, which helped in determination of MT polarity. Subtomogram averaging was performed in STOPGAP (v.0.7.3).[28] An initial reference was first generated de novo from a tomogram containing MTs that have the same polarity orientations. 10,276 subtomograms were extracted from the oversampled positions using 4x binning (7.84 Å/pixel) and a box size of 64 px^3. A starting reference was generated by averaging all subtomograms. Several rounds of alignment of the in-plane angle were conducted with shift refinements limited to 4 and 6 nm in x- and y- direction along the filament center line. This averaging approach resulted in a satisfactory MT reference. We used this optimized starting model for refining the whole dataset comprising 47 MTs from 21 tomograms sequentially at 4x binning (6 iterations), 2x binning (5 iterations), and 1x binning (5 iterations). MT polarity orientations were determined by averaging each MTs separately using multiclass averaging in STOPGAP, and subtomogram orientations were visualized in Chimera[165] as lattice maps using the Place Object plugin.[183] Polarities were sorted out using visual inspection of the tubulin radial skew,[184] then all MTs were unified to the same polarity by 180° change of the in-plane angles in the motive list. In a few occasions, radial skew could not be determined unambiguously (Figure S6D), and therefore, these MTs were discarded. Finally, 27,251 unbinned subtomograms (1x binning, 1.96 Å/pixel) were extracted using a box size of 96 pixels^3 and aligned iteratively, resulting in a refined map of a MT at a global resolution of ~9 Å (Figure S6E). The coordinates were then imported into Warp, extracted at 4x binned pixel size and subjected to 3D classification and refinement in RELION-4,[171] followed by refinement in M.[31] In total, 4 rounds of refinement were performed, gradually adding parameters: tilt-series/tomogram 2D/3D geometry, particle poses, stage angles, CTF grid search and defocus. Each M refinement round was cycled with a 3D refinement in RELION-4. In the final two rounds of M refinement, dose fractions were refined in addition to previous parameters. Finally, the last 3D refinement using 1.25x binned subtomograms was performed in RELION-4, yielding an STA map at 4.7 Å overall resolution (Figures 4D and S6F–S6H).

STA: Clathrin

Initial clathrin positions and orientations were determined using template matching with the GPU-accelerated PyTom package[30,179] (Figures S7A and S7B). The angular search was conducted with a 3-degree step against 94 4x binned tomograms. One of the published EM maps of a clathrin hub (EMD-0122),[115] low pass filtered to 15.7Å (Nyquist at 4x binning) in an 80-pixel box (7.84 Å/px), was used as a template. To minimise the number of false positives, membranes were masked out using MemBrain-seg membrane segmentations.[49] Remaining false positive picks were manually removed using the ArtiaX package[155] for ChimeraX.[185] Picks that did not form a characteristic clathrin lattice (Figure 5B) were considered false positives. This yielded 5999 clathrin triskelia. Aligned tilt-series and particle coordinates were transferred to Warp (v1.0.9),[167] where CTF estimation was performed, and subtomograms, along with the corresponding per-particle CTF models, were extracted at 3x binning (5.9 Å/px). Subsequent refinement of clathrin triskelion was carried out in RELION (v3.0) producing a 20 Å-resolution initial STA map (Figure S7C). The refined coordinates and orientations of the particles were used to refine the tilt-series alignment in M (v1.0.9).[31] New subtomograms were extracted at 2x binning (3.92 Å/px), and particle positions were refined in RELION resulting in a 12 Å map. These particles were transferred back to M for another round of refinement of the tilt-series alignment. New subtomograms were then extracted at 1x binning (1.96 Å pixel size), and particle positions were refined in RELION, yielding a 9.5 Å map (Figure S7D). The particles were once more transferred to M for symmetry expansion (C3 to C1, yielding 17,997 particles) and multispecies co-refinement with 80S ribosomes, resulting in the final STA map of clathrin at 8.7 Å resolution (Figures 4E and S7E–S7G). Refining selected classes from 3D classification did not achieve a higher resolution, hence all particles were used for the final reconstruction.

STA: Photosystem II

Particles were first picked by template matching using GPU-accelerated PyTom (pytom-match-pick)[30,179] on 4x binned CTF phase-flipped tomograms, using 7 degree rotational search with a template map generated from PDB: 6KAC, low-pass filtered to 15.68 Å (Nyquist at 4x binning). Visual inspection revealed that this template matching procedure was unable to pick some obvious PSII particles (Figure S8F), likely due to the relatively small soluble portion of PSII protruding out of the thylakoid membranes. Subsequently, a generalized 2.5D U-net was trained to segment PSII in four 4x binned tomograms using Dragonfly[95] (Figures S8A–S8D). Initial X, Y, Z coordinates of PSII positions were extracted as the center-of-mass from separate segmented instances of the U-net binary map, resulting in 26,827 initial coordinates. Thylakoid membranes were then segmented from the tomograms using MemBrain-seg.[49] The normal angle of each particle with respect to the membrane surface was assigned using a custom Python script, and particle positions were projected onto the membrane to obtain an initial alignment and angle assignment (Figure S8E). Particles picked at a distance of more than 78.4 nm from the membrane were discarded. Based on these coordinates and assigned angles, 22,895 subtomograms were extracted as 4x binned subtomograms in STOPGAP.[28] Particles were classified into 4 classes (Figure S8G), allowing for alignment with full in-plane rotational sampling, using an alignment mask focused on the luminal densities of PSII. Positions and angles from the class corresponding to PSII (13.6%, 3122 particles) were then ported into RELION-4.[171] The structure was refined with C2 symmetry and a shaped mask focused on the PSII core proteins. Per particle CTF refinement and Bayesian polishing of the tilt-series alignment were performed on 1x binned subtomograms. The refined structure was filtered to the final 19 Å resolution, as determined by the 0.143 FSC threshold from independently refined half-maps[186] (Figures 4B and S8H–S8J).

STA: ATP synthase and multispecies refinement with 80S ribosome

Nine tomograms reconstructed using IMOD, as elaborated in the pre-processing section, were used for initial processing. Template matching was performed in STOPGAP using 8x binned (80S ribosome) and 4x binned (ATP synthase) tomograms. Initial templates were generated by the simulate function of the cisTEM package, using pdb models: 6gqv (80S ribosome)[174] and 6rd4 (ATP synthase).[122] The template matching settings were as follows: lowpass filter to 31.4 Å and 15.7 Å (the respective Nyquist frequencies) and angular scanning of 15° and 12°, respectively. For the 80S ribosome, subtomogram averaging in STOPGAP was performed using 8x binned subtomograms to obtain a reference used for template matching of the whole dataset. For ATP synthase, 3D classification without alignments was performed in STOPGAP using 4x binned subtomograms. Multiple classes for ATP synthase as well as membrane mis-picks were used for the subsequent template matching scheme on the whole dataset to suppress false positives (Figures S9A–S9J). Next, 261 tomograms of mitochondria were selected for further processing. Raw EER frames were converted to TIFF stack containing 5 dose fractions using RELION-4. Motion correction and CTF estimation was performed on the TIFF stacks in Warp 1.0.9.[167] Tilt-series metadata in mdoc format and tilt-series alignments from AreTomo were imported into Warp to reconstruct tomograms at 8x and 4x binning. Template matching was performed using the GPU-accelerated implementation of PyTom[30,179] using 8x binned (80S ribosome) and 4x binned (ATP synthase) tomograms, with the following settings: lowpass filter 31.4 Å and 15.7 Å (the respective Nyquist frequencies), and angle scanning of 11° and 7°, respectively. For ATP synthase, a scoring function to remove the background false-positives from membrane-localized hits was generated in Matlab R2022b by multiplying the score map obtained for the ATP synthase class (Figure S9E, class II) by filtered score maps of the membrane-containing classes (Figure S9E, classes III & IV). Details of the scoring function, including an example, are shown in Figure S9J. Using the positions determined by template matching, subtomograms were extracted in Warp at 4x binning in both cases and used for 3D refinement in RELION-4. Subsequently, the respective species for multiparticle refinement were created in M.[31] Masks were prepared by binarization of shaped masks created in RELION. In total 5 rounds of multispecies co-refinement of ATP synthase and 80S ribosomes were performed, gradually adding up refinement parameters. In the initial round, only tilt-series/tomogram 2D/3D geometry was optimized. Up to this point, C2 pseudo-symmetry was used in all processing steps with ATP synthase (see 4x binned STA maps in Figures 5D, 5E, and S9K). Next, subtomograms of ATP synthase were extracted at 1.6x binning, the particle list was symmetry-expanded (C2 to C1; doubling the number of particles), and 3D refinement was performed in RELION-4[171] using a mask focused on the peripheral stalk. 3D classification was then performed in RELION-4 to exclude lower-quality particles, followed by another round of 3D refinement. ATP synthase species was then re-imported for a second round of multispecies co-refinement in M, CTF parameters were refined in addition to geometry using a tight binary mask around the peripheral stalk for ATP synthase. Next, subtomograms were extracted at 1.25x binning and 3D refinement was performed in RELION-4. The refined ATP synthase species was reimported to M, and masking of 80S was changed from the whole ribosome to only the large subunit. Using the updated species, two rounds of co-refinement were used to optimize the motion correction in TIFF dose fractions in addition to previously refined parameters. In the next iterative cycle, 1.25x binned ATP synthase subtomograms were extracted, followed by 3D refinement in RELION-4. At this point, we performed 3D classification masking the head domain in an attempt to resolve rotational states (Figure S9L). One class after further 3D refinement yielded a map at 8.6 Å (~11,000 particles), where densities in the head domain were resolved (Figure S9). In the final refinement in M, we used all of the previous options except refinement of motion in dose fractions. Then, particle coordinates were re-centered at a single ATP synthase monomer and unbinned subtomograms were extracted from M. Finally, 3D classification and 3D refinement were performed in RELION-4, yielding a structure of the peripheral stalk at 5.2 Å (~88,000 particles) (Figure S9N). 80S ribosome particles (Figure S9O). were subjected to 3D refinement in RELION-4 only once and all consecutive refinements were performed in M during the 5 rounds of multispecies refinement with ATP synthase. Finally, a composite map was made by combining the average of the head domain with the average of the peripheral stalk (Figures 4F, 5F, and 5G).

Data structure of the deposition on EMPIAR

The 28 TB of EMPIAR-11830 have been deposited with the following data structure (see Figure S10). The data are partitioned into three image sets, one containing a minimal TOMOMAN project,[169] the second containing 4x binned denoised tomograms for visualization and particle picking, and the third containing 4x binned 3D CTF-corrected tomograms for template matching and direct subtomogram averaging. Each tilt-series is kept in a separate subfolder named with date of data collection, location, and microscope type. Further, each tilt-series folder is split into subfolders which include raw tilt-series and auxiliary files to provide a rapid overview. The reconstructed tomograms are numbered and contained in one single folder, and a STAR file[187] is provided that indicates numbers corresponding to the tilt-series names. We maintained the accompanying metadata according to the structure commonly used for cryo-EM datasets.

QUANTIFICATION AND STATISTICAL ANALYSIS

Statistical tests were not performed during the creation, annotation, and structural assessment of this community resource.